Max-Planck-Institut
für Meteorologie

REPORT No. 65

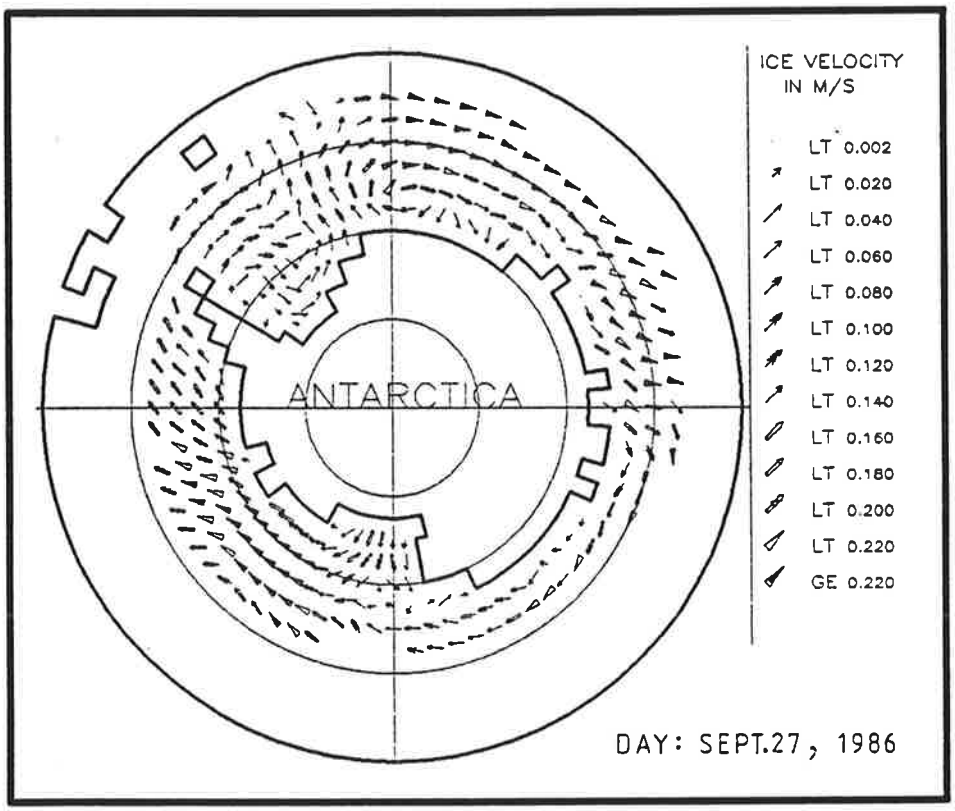

SOUTHERN OCEAN SEA-ICE SIMULATIONS FORCED WITH OPERATIONALLY DERIVED ATMOSPHERIC ANALYSES DATA

by

ACHIM STÖSSEL

HAMBURG, JUNE 1991

AUTHOR:

ACHIM STÖSSEL

MAX-PLANCK-INSTITUT
FUER METEOROLOGIE

MAX-PLANCK-INSTITUT
FUER METEOROLOGIE
BUNDESSTRASSE 55
D-2000 HAMBURG 13
F.R. GERMANY

Tel.: (040) 4 11 73-0
Telex: 211092 mpime d
Telemail: MPI.METEOROLOGY
Telefax: (040) 4 11 73-298

REPb65

Southern Ocean Sea-Ice Simulations forced with operationally derived Atmospheric Analyses Data

Achim Stössel

Max-Planck-Institut für Meteorologie, Hamburg

Abstract

As a supplement to an earlier paper on a coupled sea-ice – oceanic mixed-layer [SI – OML] model for the Southern Ocean (Stössel et al., 1990), the atmospheric forcing in this investigation is changed from monthly (climatological) data to daily (instantaneous) values. These data are derived from global analyses from the European Center for Medium Range Weather Forecasts (ECMWF). With these computations applied as surface forcing, results similar to the earlier ones are achieved. Adjustments of the SI-model parameters and/or the coefficients of the bulk formulas can be avoided when the forcing is raised to its originally assigned level, using an appropriate Prandtl-layer parameterization. With this extension, the model results are well comparable with observations based on operationally produced ice charts.

A further rise of the atmospheric forcing to the geostrophic level by means of coupling a one-dimensional atmospheric boundary-layer [ABL] model to the SI – OML model, reduces the dependency of the results on the (climatologically) prescribed boundary conditions of the operational numerical weather-prediction [NWP] model. The simulations with this extension, however, appear to be reasonable only when the surface wind pattern is applied, the roughness length over ice and water is increased, and the stability of the ABL over ice is generally reduced.

ISSN 0937–1060

1. Introduction

Dynamic-thermodynamic modelling of Antarctic sea ice was the challenge of several authors since 1979. Parkinson and Washington (1979) modelled the sea ice around the entire continent with highly sophisticated thermodynamics but rather crude dynamics. Hibler and Ackley (1983) employed a sophisticated ice rheology for the dynamics but restricted the thermodynamics as well as the domain, the latter describing the Weddell Sea region. This model has been extended to include a prognostic OML by Lemke et al. (1990), a prognostic snow layer by Owens and Lemke (1990), and independently, a diagnostic ABL by Koch (1988). With the first two extensions, the Weddell Sea model has finally been enlarged to simulate the entire Southern Ocean ice pack by Stössel et al. (1990) (in the following referred to as SLO).

Sea-ice models coupled to oceanic general circulation [OGC] models with application to Antarctic sea ice were constructed by van Ypersele (1986) employing an ocean model based on the primitive equations (Bryan, 1969; Semtner, 1974), sea-ice thermodynamics similar to Parkinson and Washington (1979) (Semtner, 1976) and sea-ice dynamics based on free drift assumptions (Thorndike and Colony, 1982). Oberhuber (pers. communication) developed a global OGC model with isopycnic coordinates (Oberhuber, 1991), which includes comprehensive mixed-layer dynamics and a sophisticated sea-ice model based on Semtner (1976) for the thermodynamics and on Hibler (1979) for the dynamics. Other OGC models which include Antarctic waters suffer from the neglection of either comprehensive ice thermodynamics (Maier-Reimer and Mikolajewicz, 1989; Manabe et al., 1990) or ice advection, where in the latter case, however, ice compactness may be prognostically determined (e.g. Foreman et al., 1988).

Except for the SI models restricted to the Weddell Sea, the atmospheric forcing generally consists of monthly values from climatologies. Since measurements in the Southern Ocean are rather sparse, the quality of these data mainly depend on the analyses techniques. A physically more consistent representation of the atmospheric variables is believed to be represented by analyses from operational NWP centers, which consist of a blend of

instantaneous measured data and modelled values of the previous forecast run.

When using data from the lowest level of these analyses, however, a significant influence of the specified lower boundary conditions of the atmospheric general circulation [AGC] model on the variables of the lowest layer is to be expected. In the case where the prescribed sea-surface temperature [SST] for the open sea is replaced by ice-surface temperatures [IST] in ice covered regions, there is a huge impact on the variables in this layer, especially on temperature and humidity. Since the IST's, together with the ice edge, are usually specified from climatologies, the lower layer AGC model variables are correspondingly biased. To avoid a corresponding predetermination when using the AGC model computations as forcing fields, an attempt is made to raise the atmospheric forcing level of temperature, humidity and wind to the next higher one of the analyses, i.e. 850 hPa, in accordance with Koch (1988).

As sea ice strongly interacts thermodynamically as well as dynamically with atmosphere and ocean, it seems to be adequate to include sophisticated SI models in coupled AGC – OGC models. In spite of the fact that the coupling of the present SI model is restricted to the boundary layers of the neighboring media, which themselves are restricted to vertical processes, the present investigation can be regarded as a prestudy to a three-dimensional coupling of the three spheres.

In the next section, the SI – OML model will be described briefly. This is followed by a description of the forcing data, with emphasis on the daily data of the NWP-center's analyses. The results are presented in steps following an ABL-coupling hierarchy. First, the results with direct surface forcing will be demonstrated. Next, the SI – OML model is extended by an atmospheric surface-layer [ASL] (Prandtl-layer) parameterization. Finally, the SI – OML model is coupled to the ABL model mentioned above. Since the results of the latter version are not automatically satisfactory, they are analyzed in a series of sensitivity studies.

2. Basic Model

The SI – OML model used in this study is identical to the one used in SLO. The SI model is based on Hibler (1979) employing a viscous-plastic ice rheology for the calculation of the force due to variations in internal ice stress, $F_k = \partial\sigma_{kl} / \partial x_l$, which is part of the momentum balance and where σ_{kl} is the two-dimensional stress tensor. The dynamic and the thermodynamic parts of the SI model are combined in continuity equations for ice thickness (h_i), ice compactness (N_i) and snow thickness (h_{sn}) according to Owens and Lemke (1990). The continuity equation of ice compactness is supplemented by an additional dynamic term according to Hibler (1984), which allows for the creation of extra open water due to shear deformation and is energetically consistent with the elliptical yield curve in principal component stress space, which determines the ratio of compressive to shear strength (Leppäranta and Hibler, 1985).

The thermodynamic part of the SI model is based on the calculation of the heat balance over the ice free and ice covered part of the grid cell, similar to Semtner (1976) and Parkinson and Washington (1979). Over sea ice one yields

$$(1 - \alpha)\, Q_{sw} + Q_{lw} - \varepsilon\sigma T_s^4 + Q_{se} + Q_{la} + Q_c \equiv Q_a + Q_c = 0 \quad , \qquad (1)$$

where
- α : albedo (freezing or melting ice or snow),
- Q_{sw} : heat flux due to short wave radiation,
- Q_{lw} : heat flux due to long wave radiation,
- ε : emissivity,
- σ : Stefan-Boltzmann constant,
- T_s : surface temperature (ice or snow),
- Q_{se} : sensible heat flux,
- Q_{la} : latent heat flux,
- Q_c : conductive heat flux,
- Q_a : atmospheric heat flux.

When the atmospheric forcing is applied at the surface, the radiative and turbulent heat fluxes are calculated by standard or bulk formulas, respectively (e.g. Parkinson and Washington (1979), van Ypersele (1986)). The albedo varies according to the presence of snow and the sign of thermodynamic ice growth. For the

conductive heat flux one obtains

$$Q_c = \frac{(T_b - T_s)\, k_i}{\tilde{h}_i} \quad , \tag{2}$$

where T_b : temperature at the ice bottom (= freezing point),

k_i : thermal conductivity of ice,

and

$$\tilde{h}_i = \hat{h}_i / N_i \quad , \tag{3}$$

which represents the "effective" ice thickness with

$$\hat{h}_i = h_i + h_{sn} \frac{k_i}{k_{sn}} \quad , \tag{4}$$

where k_{sn} is the thermal conductivity of snow and $\hat{h}_i$ the "total" ice thickness. For the ice covered part of the grid cell the heat-balance equation can now be calculated with the locally existing effective ice thickness (3). The thermal isolation of snow is implicitly accounted for by the total ice thickness (4), where the actual snow thickness is transfered into an equivalent ice thickness (Owens and Lemke, 1990).

T_s is solved by iteration of (1). If the surface temperature is above freezing, T_s is set as 0°C, with (1) being equal to $-\rho_i L_f (\partial \tilde{h}_i / \partial t)_s$, according to Maykut (1982). The surface melting is then calculated as:

$$\left(\frac{\partial \tilde{h}_i}{\partial t}\right)_s = \frac{1}{\rho_i L_f} (-Q_a - Q_c) \quad , \tag{5}$$

where ρ_i : density of sea ice,

L_f : latent heat of fusion.

At the bottom of the ice the melting or freezing rate is determined from

$$\left(\frac{\partial \tilde{h}_i}{\partial t}\right)_b = \frac{1}{\rho_i L_f} (Q_c - Q_o) \quad , \tag{6}$$

where Q_o is the oceanic heat flux. Thus, the change of the effective ice thickness is given by

$$\left(\frac{\partial \tilde{h}_i}{\partial t}\right) = \left(\frac{\partial \tilde{h}_i}{\partial t}\right)_b + \left(\frac{\partial \tilde{h}_i}{\partial t}\right)_s \quad , \tag{7}$$

where the last term on the right-hand side applies only when $T_s = 0°C$.

An additional modification to Hibler and Ackley (1983) has been adopted by using a seven-level ice-thickness parameterization for the thermodynamic part according to Hibler (1984):

$$\left(\frac{\partial \tilde{h}_i}{\partial t}\right) \equiv w_i(\tilde{h}_i) = \frac{1}{n}\sum_{k=1}^{n} w_i\left(\frac{(2k-1)\tilde{h}_i}{n}\right) \quad , \tag{8}$$

where $n = 7$ and $w_i(\tilde{h}_i)$ the ice growth rate for thickness $\tilde{h}_i$. With this formula, the heat-balance equation is solved for seven ice-thickness categories in order to account for the highly non-linear relationship between growth rate and ice thickness.

The comprehensive thermodynamic terms for all three continuity equations are shown in Owens and Lemke (1990).

The OML model is based on Lemke (1987) and was coupled to the SI model described above by Lemke et al.(1990). It consists of conservation equations for heat and salt, and resolves the base of the mixed layer with an exponentially shaped pycnocline. In order to parameterize the entrainment, the following assumption is made:

$$\frac{\partial T_{o1}}{\partial t} = \left(\frac{Q_a}{\rho_a c_a} + \frac{Q_o}{\rho_o c_o}\right) / h_{o1} \equiv \left(\tilde{Q}_s + \tilde{Q}_e\right) / h_{o1} \quad , \tag{9}$$

where T_{o1} : mixed-layer temperature,
ρ_a : air density at the surface,
c_a : specific heat capacity of air,
ρ_o : sea-water density at the surface,
c_o : specific heat capacity of sea water,
h_{o1} : mixed-layer depth,

i.e., the local change in mixed-layer temperature is composed of the atmospheric and oceanic heat flux. The latter is defined as the entrainment heat flux and parameterized as:

$$\tilde{Q}_e = (\overline{T}_{Tc} - T_{o1})\, w_e \quad , \tag{10}$$

with

$$\overline{T}_{Tc} = \frac{1}{\delta'}\int_{-h_{o1}-\delta'}^{-h_{o1}} T_o(z_o)dz_o = T_{o2} + (T_{o2} - T_{o1})h_{Tc}\left(\exp\left(\frac{-\delta'}{h_{Tc}}\right) - 1\right)/\delta' \quad ,$$

where w_e : entrainment velocity,
δ' : turbulent length scale,

z_o : depth,

T_{o2} : temperature at the base of second oceanic layer,

h_{Tc} : thermocline thickness.

This is a modification to the Kraus-Turner type parameterization in the sense that the entrainment heat flux is not directly dependent on T_{o2}, but rather on a mean temperature within the entrainment zone ($\overline{T}_{Tc}$), which is prognostically determined. This formalism is analogous for salinity.

For the coupling with sea ice it is assumed that T_{o1} remains at the freezing point when sea ice is present, i.e. $\partial T_{o1}/\partial t = 0$. Thus, the surface heat flux yields:

$$\tilde{Q}_s = -\tilde{Q}_e \quad . \tag{11}$$

To determine the surface salt flux ($\tilde{S}_s$), it is assumed that this is composed of the freezing or melting rate derived from the conductive and oceanic heat fluxes, and the net fresh-water flux due to precipitation and evaporation:

$$\tilde{S}_s = (S_1 - S_i)\left(\frac{\partial h_i}{\partial t}\right)_{th.} \frac{\rho_i}{\rho_o} - FS_1 \quad , \tag{12}$$

where S_1 : mixed-layer salinity,

S_i : sea-ice salinity,

ρ_i : sea-ice density,

F : net fresh-water flux,

and where $(\partial h_i/\partial t)_{th.}$ is the thermodynamic change of the mean ice thickness within a grid cell, (i.e. including ice-thickness growth due to new-ice production). The fresh-water flux is modified by the presence of snow according to Owens and Lemke (1990).

Finally, to close the system of equations (i.e. to determine the entrainment velocity in (10)), the potential energy due to the surface and entrainment heat and salt fluxes ($\tilde{Q}_s$, $\tilde{Q}_e$, $\tilde{S}_s$, $\tilde{S}_e$) is supposed to be balanced by the kinetic energy produced by the wind drag and the ice drift, respectively, and in winter additionally by convection (Lemke et al., 1990).

The variables involved in the SI – OML model are illustrated in Fig. 1. They are distinguished between diagnostically computed ones, prognostically computed ones and those which are externally specified (forcing variables). The explanations of the symbols are

found in the notation list. The temperature and salinity profiles indicated by full lines are supposed to represent a winter situation with a deep mixed layer, which is colder and slightly less saline than the layer below the pycnocline, thus representing a stratification, which is only marginally stable (Martinson, 1990). In summer (dashed profiles), h_{o1} is shallower, $T_{o1} > T_{o2}$ and the salinity is less than in winter, due to ice melt, which together with the warming of the mixed layer generally leads to a stable stratification with h_{o1} being diagnostically determined by the Monin-Obukhov length.

According to SLO, the model is run on a spherical, circumpolar grid with a latitudinal resolution of 2.5° and a longitudinal resolution of 5°, extending from 50°S to 80°S. An integration time of 6 years is employed together with a daily time step.

3. Forcing Data

Except for the atmospheric variables such as temperature, humidity and wind, the forcing in terms of cloudiness, geostrophic currents, as well as temperature and salinity at the base of the second oceanic layer is specified from climatologies and identical to that used in SLO for the standard run. An exception is the precipitation rate, which is presently taken from the Jaeger (1976) grid-point data. Since the sensitivity of the former simulations to this alternative precipitation forcing was rather low (SLO), no significant impact on the present results is expected.

To force the SI – OML model with daily variables it is not possible to refer to actual observations, as in the Southern Ocean region the corresponding network is too coarse compared to the resolution of the model. To investigate the first order effects of daily variability a stochastic forcing with observed variability was introduced in SLO. On the other hand, daily atmospheric data are available from AGC models, which, under certain conditions, can be used to force sea-ice models.

For this purpose it seems to be useful to employ analyses results of the data-assimilation phase of an operational NWP model, where actual observations and measurements are included. In

the case of a coarse observing network the analyses are strongly influenced by the previous forecast (Heimann, personal communication; Trenberth and Olson, 1988). This has an enormous advantage compared to climatological analyses which are purely based on observations. While in the latter case, observation gaps are filled up by spatially and temporally interpolated values, the forecast results are spatially consistent with the patterns of the large-scale circulation and a product of the temporal evolution on the synoptic scale.

The employment of the analyses data as surface forcing fields, however, is generally not uncritical (see e.g. Cattle and Roberts, 1988), and it must be emphasized that for the present region these data are primarily simulation results of an atmosphere model, which themselves can be erroneous. Another disadvantage appears to be the fact that during their evolution the NWP models were continuously improved parallel to their operational application. Thus, the presently available data sets covering several years are based on different model versions (Bengtsson and Shukla, 1988) and are consequently not entirely consistent.

In the present study, computations of the global analyses of the ECMWF have been used, which are prescribed on the standard pressure levels. They cover the years 1980-1987, with a resolution of 2.5° x 2.5° in space and 12 h in time (Trenberth and Olson, 1988). From this data set the variables temperature, relative humidity, wind and geopotential height from the 850 hPa and 1000 hPa pressure levels were extracted for the years 1985 and 1986.

The data are spatially (horizontally) interpolated to the model grid and are converted into daily mean values in order to be commensurate with the model time step. Since the integration time is six years, the first five years were forced with data from the year 1985, while the sixth year is determined by the 1986 forcing. The model results, which are presented in the following sections, will thus represent this final year of model integration, i.e. the year 1986.

4. Results with atmospheric surface forcing

Since the lowest level of the analyses is at 1000 hPa, temperature and humidity are interpolated to the surface (or 2 m height) following the ECMWF Research Department (1986). The surface pressure is calculated using the geopotential height at 850 hPa and 1000 hPa as well as the temperature and specific humidity at 1000 hPa according to Trenberth and Olson (1988). Since in the ECMWF assimilation scheme wind observations at sea level were directly implemented as 1000 hPa winds before 9.9.1986, they are presently used as surface winds without correction for height following Trenberth et al.(1989) and Janssen et al.(1989).

The purely model derived, diagnostic atmospheric surface (i.e. 2 m or 10 m) variables (archieved in the so called TOGA data set, also available at the ECMWF), were not employed in the present study. This is mainly due to the fact that these variables are highly dependent on the treatment of the ABL during the postprocessing phase. In ice covered regions, however, the ABL processes are relatively unknown. Additionally, the results are expected to be crucially dependent on the specified lower boundary conditions of the AGC model, i.e. poleward of the predominantly climatologically determined ice edge by climatological IST's (ECMWF Research Department, 1986). In these regions, a grid cell is assumed to be either totally ice covered or ice free, thus additionally ignoring any effects arising from partially ice covered grid cells.

Using the forcing configuration described above, without any adjustments of the model parameters as compared to the standard version in SLO, the spatial ice-thickness distribution (being the most crucial indicator for the skill of sea-ice simulations) was rather similar to the one obtained with monthly forcing from climatologies (see Stössel, 1991). The main differences compared to observations were a slightly overestimated winter ice extent and a general overestimation of the compressions in convergent ice areas.

These deficiencies can be overcome in an ad hoc manner by simultaneously adjusting the sea-ice model parameter P^*, which affects the ice strength, and the drag coefficient for the

calculation of the wind stress. In the experiment mentioned above the 1000 hPa wind, which is supposed to represent the surface wind, was treated as a geostrophic wind with respect to the drag coefficient ($C_{da} = 1.2 \cdot 10^{-3}$). According to McPhee (1980) and Leppäranta (1981), however, this coefficient, when used in conjunction with surface (or 10 m) winds, should be specified by a ratio 1 to 2 to the corresponding drag coefficient between ice and ocean (C_{do}). Thus with $C_{do} = 5.5 \cdot 10^{-3}$ it follows that $C_{da} = 2.7 \cdot 10^{-3}$ for the 10 m wind (see also Overland, 1985).

With such a modification, the ice is expected to encounter too much ridging in regions with convergent ice drift. Therefore, additionally, the ice-strength parameter has been increased by a factor of 5.5 proposed by Hibler and Ackley (1983) for the application of daily wind forcing.

In summary, the higher drag coefficient is introduced because of the employment of surface winds instead of geostrophic winds, while the higher ice strength accounts for the use of daily winds instead of monthly means.

The resultant ice-thickness distribution is shown in Fig.2 for the approximate date of minimum (a) and maximum (b) ice extent, where "day 60" corresponds to 1.3.1986 and "day 270" to 27.9.1986. The most significant difference to the earlier result without adjustment (Stössel (1991): Fig.1), is the highly reduced ridging in convergent ice areas. Here the increased ice strength exerts a higher effect than the increased stress between the ice and the atmosphere. The maximum ice thickness in the Weddell Sea attains 4.2 m instead of 7.5 m, which appears to be more realistic. The area of the thicker ice ($h_i > 1.5$ m), on the other hand, hardly changed. This is also true for the ice compactness, except for the Ross Sea in summer, where the ice totally disappears.

Fig.3.a shows the corresponding ice drift in winter for the 27.9.1986, i.e. for an instantaneous date, while Fig.3.b represents the monthly mean of this variable for September. In the daily plot, the ice drift is dominated by an extensive anticyclonic gyre in the Weddell Sea. Ice velocities of almost 30 cm/s are achieved even in compact, but divergent, ice fields (Amundsen Sea at 70°S), which approach values of free ice drift (see e.g. Hoeber and Gube-Lehnhardt, 1987). The structure of the

monthly mean ice drift (Fig.3.b) corresponds essentially to the results obtained by the standard run with climatological (monthly mean) forcing in SLO, with the characteristic (cyclonic) Weddell gyre, the strong offshore ice drift in the Ross Sea and several smaller gyres along the coast of east Antarctica.

In Fig.4, the seasonal cycles of ice extent and ice volume as simulated with the present model version and forcing (thick curves) are demonstrated in comparison to the correspondent standard ones presented in SLO (thin curves). Discrepancies occur primarily in summer, where the ice extent is now reduced by about $3 \cdot 10^6$ km^2 and the ice volume by about $6 \cdot 10^3$ km^3. While the maximum ice extent in winter is smaller as well, the duration of the winter (defined as the accumulated time during which the instantaneous extent is higher than the annual mean extent) is longer with respect to this variable by about one month. The asymmetry in period towards "longer winter" (about 7 months) and "shorter summer" (about 5 months) can also be recognized in the observed seasonal cycles (Lemke et al., 1980; Zwally et al., 1983).

Fig.5 shows the contours of the mixed-layer depth and corresponds to Fig.5 in SLO. The higher wind variability and the larger drag coefficient lead to a higher ice drift in the divergent ice field and thus to an increased turbulent kinetic energy input into the ocean. Accordingly, the equilibrium depth of the mixed layer in summer (Fig.5.a), which is determined by the Monin-Obukhov length, increases to about twice the amount registered with the monthly mean wind forcing (compare with Fig.5.a in SLO). The deep mixed-layer anomaly in the south-western part of the Weddell Sea in summer is related to relative cold air temperatures at exactly this location with a simultaneous slow ice drift. This prevents the ice from melting and, consequently, the stratification below the ice from stabilizing. In winter, the mixed-layer depth is deeper by about 40 m compared to the earlier results. This is in remarkably good agreement with observations, at least in locations where these are available as e.g. from the Winter Weddell Sea Project 1986 along the Greenwich meridian (Martinson, 1990; Gordon and Huber, 1990). New areas of deeper mixed layers occur in the Bellingshausen and Amundsen Seas.

Compared to the climatologically forced experiment (SLO: Fig.6), differences in the pattern of the mean oceanic heat flux (Fig.6) are restricted to single locations, whereas the magnitude has increased globally by about a factor of four. The area of positive net freezing rate has expanded considerably to the north in the Weddell Sea as well as in the Ross Sea (Fig.7 versus Fig.13 in SLO) and the local melt rates are strongly increased. On the one hand, these features are related to the higher turbulent heat fluxes due to the introduction of daily variability. On the other hand, they can be explained by the higher variability of ice drift, leading to more frequent occasions for new-ice production in winter with a subsequent extension of the area of positive net freezing rates and a squeezing of the area of net melting. Since, on average, the thermodynamic forcing fields are rather similar, their influence can be neglected.

5. Extension with ASL model

5.1 Model description

It will be demonstrated in the following experiment that realistic results can also be achieved without changing the ice-strength parameter. This parameter essentially modifies the simulation in convergent ice drift areas with high ice compactness and thickness. Altering the wind forcing from monthly or weekly mean values to daily ones, however, also affects the divergent parts of the ice pack, which in the Southern Ocean region are the prevailing ones. Thus, when the wind forcing is changed to higher variability, which consequently leads to higher stress, a compensation is needed for the overall ice pack. This is provided in the following by atmospheric surface-layer considerations. To describe the next experiment, it is first necessary to analyze the forcing fields.

The reasoning of Trenberth et al.(1989) for the employment of the 1000 hPa winds as surface winds is based on the fact that surface wind observations and measurements were directly assimilated as 1000 hPa winds (see section 3). However, since observations are hardly available in the Southern Ocean, the applied analyses data are primarily model derived. Therefore, in

the following the assimilation of the model computations into the analyses will briefly be explained.

As described in section 3, the lowermost variables of the global analyses are prescribed at the standard pressure levels 850 hPa and 1000 hPa, respectively (Trenberth and Olson, 1988). These levels, however, do not coincide with the vertical grid of the atmosphere model, which is hybrid with a finer resolution in the lower levels, the lowest one representing a height of about 30 m. In the analyses, the computations at the model grid are interpolated to the standard pressure levels. If the 1000 hPa level lies beneath the lowest model level, the 1000 hPa temperature is determined via the lapse rate, the relative humidity via linear extrapolation and the wind without height correction from the lowest model value (ECMWF Research Department, 1986; see also Heimann and Monfray, 1991).

Recalculating, for the latter case, temperature and humidity of the 1000 hPa level to the lowest model level ($\approx$ 30 m) and employing the "1000 hPa winds" as 30 m winds, which they are originally, and otherwise using the 1000 hPa values together with their instantaneous height, the turbulent heat fluxes (transfer coefficients) and the stress over ice (drag coefficient) can be determined via the employment of an ASL parameterization.

The parameterization of the atmospheric surface layer used here corresponds to the one employed in the AGC model of the ECMWF (ECMWF Research Department, 1985) and refers to Louis (1979). It is based on the Monin-Obukhov theory, where the Monin-Obukhov length is replaced by the bulk Richardson number of the lowest atmosphere layer:

$$Ri = gz_{a1}(\theta_{a1} - \theta_s + 0.61\theta_s(q_1 - q_s))/(\theta_s|\vec{V}_{a1}|^2) \quad , \qquad (13)$$

where g : acceleration due to gravity,

z_{a1} : height of the first (lowest) atmosphere layer,

θ_{a1} : pot. temperature of the first atmosphere layer,

θ_s : potential temperature at the surface ($\approx T_s$),

q_1 : specific humidity of the first atmosphere layer,

q_s : specific humidity at the surface,

$\vec{V}_{a1}$: wind in the first atmosphere layer.

In the original application (Louis, 1979) the lowest atmospheric

level is determined by the lowest AGC model level (≈ 30 m), whereas in the present application z_{a1} increases when the surface pressure exceeds 1004 hPa, i.e. the 1000 hPa level lies above the lowest model level.

The friction velocity (u_*) is defined from the vertical eddy flux of momentum:

$$\overline{w'u'} \equiv u_*^2 = F'_m \left(\frac{\kappa}{\ln(z_{a1}/z_s)} \, |\vec{V}_{a1}| \right)^2 , \qquad (14)$$

where κ : von Karman constant,

z_s : roughness length,

F'_m : stability function for momentum transfer.

Correspondingly, the scaling temperature (θ_*) is supposed to be related to the vertical eddy flux of sensible heat:

$$-\overline{w'\theta'} \equiv u_*\theta_* = -\frac{Q_{se}}{\rho_a c_a} = \frac{\kappa^2 |\vec{V}_{a1}| (\theta_{a1} - \theta_s) F'_h}{0.74 \ln^2(z_{a1}/z_s)} , \qquad (15)$$

where F'_h is the stability function for the turbulent heat flux. The latent heat flux is given by an analogous formula with q_1 and q_s.

The stability functions for neutral and convective stratifications follow from analytical adaptations to the functions of Businger et al. (1971). In the case of highly stable stratifications, an expression for $F'_{m,h}$ is adopted which allows for an approach towards an asymptote at high Ri-values in order to avoid an energetic disconnection of the surface from the atmosphere.

In accordance to the ECMWF model the roughness length over sea ice (z_{si}) is $1 \cdot 10^{-3}$ m and that over ice-free waters (z_{so}) determined by Charnock's formula via the friction velocity, where the Charnock constant is specified with 0.032 m.

5.2 Results

Fig. 8 shows the resulting ice-thickness distribution for the same dates as in Fig. 2. In spite of the low P^*-value the results are rather similar to the ones of the previous experiment (Fig. 2). Contrary to the latter, convergent drift regions are more pronounced. On the other hand, they show fairly reduced

compressions as compared to the experiment without adjustment of P^* and C_{da} (Stössel, 1991: Fig.1). Although the thicknesses are difficult to verify, the present results seem to be the most realistic ones.

For the present experiment a sequence of the real-time areal distributions of ice compactness for the year 1986 is demonstrated in Fig.9 in intervals of about 3 months. Fig.10 presents slightly modified copies of operational ice charts (Navy/NOAA Joint Ice Center, 1986), which are based on real-time observations from a variety of sources. The scale and dates are consistent to Fig.9. The simulation results appear to be generally reasonable. The summer ice extent, which usually is the most difficult one to simulate, shows too low ice concentrations in the north-western part of the Weddell Sea, in the eastern parts of the Ross Sea, and in the Amundsen Sea (Fig.9.a). Keeping in mind the relatively low resolution of the ice model, the period of ice advance (Fig.9.b) is simulated satisfactorily, with a slight overestimation in the north-eastern part of the Weddell Sea. The winter compactness (Fig.9.c), too, essentially agrees with observations, although the extent is overestimated in some sectors. The high concentrations ($N_i > 80\%$) beyond the marginal ice zone (MIZ) in Figs.9.b and 9.c are striking. These, as well as the width of the MIZ of $\Delta\varphi \approx 1^\circ - 3^\circ$, correspond to observations (Figs.10.b and 10.c; compare also Wadhams et al., 1987). The process of ice break-up in spring is also reasonably well simulated (Fig.9.d). It starts in the Indian Ocean sector, which is consistent with the observations (Fig.10.d). Coastal polynyas can be identified by lower concentrations along the continent. The observed polynya in the southern Ross Sea is not present in the simulation. Instead, there is a polynya in the eastern Ross Sea, which is attributed to an increased vertical oceanic heat flux due to instantaneous divergent ice drift with a simultaneous cold-air advection (from the main land).

Due to the generally lower surface stress over ice, the ice velocities in the divergent ice fields are reduced and are thus more realistic (Fig.11). The mixed-layer depth, on the other hand, is reduced in summer by 10 - 20 m (Fig.12.a) in comparison with the result from the previous run (Fig.5.a), and thus rather close

to the result with the climatological, monthly mean forcing presented in SLO (there in Fig.5.a). This feature is related to the specification of the roughness lengths, which will be discussed in section 6.2.2. The winter mixed-layer depth, which is primarily determined by the entrainment velocity, does not differ much from the previous run, except for several locations along the coast (especially in the southern Weddell Sea and in the south-eastern Ross Sea). The discrepancies at these locations are related to the reduced ice drift, which itself is attributed to the stability dependency of the ASL parameterization. This leads in the present case to an effective reduction of the turbulent energy (incl. momentum) transfer from the atmosphere to the sea ice at locations of high ice compactness and/or ice thickness. Specifically, the introduction of the ASL parameterization exerts a higher impact in terms of a reduction of the ice drift (and hence the mixed-layer depth) than the reduction of the ice strength (as compared to the previous simulation presented in section 4). As the differences in the winter mixed-layer depths (Fig.5.b versus Fig.12.b) are exclusively restricted to locations of ice divergence (compare with Fig.2), it is obvious that these locations were not particularly modified by the higher P^* value in the previous experiment. This indicates that P^* is not the appropriate adjustment parameter if the variability of the wind forcing is changed.

Correspondingly, the vertical oceanic heat flux is reduced on average by 3 to 4 W/m^2, being less commensurate with observations (Gordon and Huber, 1990) as compared with the results from the previous simulation. This demonstrates that an improvement of the sea-ice simulation does not necessarily lead to an improvement of the mixed-layer simulations. This fact can be attributed to inconsistencies in the energy transfer between atmosphere, sea ice and ocean. On the other hand, large-scale estimates of the mean vertical oceanic heat flux derived from single measurements are certainly within an error band which is comparable to the present discrepancies. This makes an absolute evaluation of the model results rather difficult.

The net freezing (and melting) rate, too, is significantly reduced due to the lower mobility of the sea ice (Fig.13).

Nevertheless, the areas of dominant freezing (and melting) are nearly identical compared to the previous run (Fig.7).

The improvements of the present results versus the previous ones without ASL parameterization are primarily due to the different determination of the turbulent heat fluxes. In the present case these are not just dependent on the vertical temperature and humidity gradients, but also on the stability-dependent friction velocity. As a consequence of this, the summer ice melt in the Ross Sea, e.g., is much weaker than in the previous experiment, where the transfer coefficient was independent of the current ice situation. There, the strength of the coupling between the specified atmospheric variables and the SI – OML model always remained the same, i.e. the results were always direct and in the same way dependent on the thermal (and mechanical) surface forcing.

6. Extension with ABL model

6.1 Model description

Assuming that a proper sea-ice model is employed, the problems of sea-ice simulations are less determined by the sea-ice model itself but instead more by the fact that the model results are very sensitive to the specified forcing, especially to the variables oceanic heat flux and wind (Stössel et al., 1990; Stössel, 1991). This leads to the conclusion that the quality of the model results is highly dependent on the quality of the forcing fields. Since the Southern Ocean region probably has the coarsest observational network on Earth, the forcing data for that region can be expected to be accordingly poor, if they are purely based on observations (see section 3).

The dependence of the model results on the vertical oceanic heat flux was in first order reduced by the coupling to the mixed-layer model, where the forcing level with respect to temperature and salinity was posed at 500 m depth.

As mentioned before, the atmospheric forcing variables in terms of temperature, humidity and wind derived from NWP-center analyses are primarily model-generated in the Southern Ocean region. The use of the values from the near-surface level of the analyses as

atmospheric forcing for the sea-ice model has a drawback as the computations of the lowermost AGC model level are highly dependent on the specified lower boundary conditions of that model (i.e. in the present case on the specified sea-ice conditions). Thus, a certain predetermination is to be expected when these computations are used as forcing data.

To circumvent this deficiency an attempt has been made to raise the forcing level of the variables mentioned above to the next higher one of the (ECMWF) analyses (850 hPa). This is presently realized by an additional coupling to a (in first order) one-dimensional ABL model, as was done by Koch (1988) for the Weddell Sea-ice model of Hibler and Ackley (1983).

With this ABL model the forcing level is raised by the entire Ekman layer. The surface layer is treated in accordance to the Monin-Obukhov similarity theory, i.e. similar to the ASL parameterization described in the previous section. Applying the Rossby-number similarity theory, the resistance laws for the barotropic Ekman layer can be derived after vertical integration of the flux-profile relationships from the roughness length z_s to the geostrophic level z_{a2}. This yields for the sensible heat flux:

$$-\frac{Q_{se}}{\rho_a c_a} = \kappa u_* (\theta_{a2} - \theta_s) \left(\ln \frac{u_*}{f z_s} - C(\mu) \right)^{-1} \qquad (16)$$

and for the momentum flux:

$$\ln \frac{u_*}{|\vec{V}_{a2}|} = A(\mu) - \ln \frac{|\vec{V}_{a2}|}{f z_s} + \left[\left(\kappa \frac{|\vec{V}_{a2}|}{u_*} \right) - B^2(\mu) \right]^{0.5} , \qquad (17)$$

where θ_{a2} : pot. temperature of the second atmosphere layer,

f : Coriolis parameter,

$\vec{V}_{a2}$: wind in the second atmosphere layer.

The latent heat flux is determined analogously to (16). A, B and C are functions of the stability parameter

$$\mu = \frac{\kappa u_*}{f L'} , \qquad (18)$$

where L′ is the Monin-Obukhov length given by

$$L' = -\rho_a c_a \frac{T_s}{g\kappa} \left(\frac{u_*^3}{Q_{se} + 0.61 T_s c_a Q_{la} / L_v} \right) , \qquad (19)$$

where L_v is the latent heat of vaporization. These stability functions are empirically determined following Fiedler and Panofsky (1972).

Additionally, the similarity theory of the Ekman layer provides the turning angle between the geostrophic flow and the stress at the surface:

$$\sin\phi_a = - \frac{B(\mu)}{\kappa} \frac{u_*}{|\vec{v}_{a2}|} \quad . \tag{20}$$

Accordingly, the stress between ice and atmosphere yields:

$$\vec{\tau}_a = \rho_a u_*^2 \frac{\vec{v}_{a2}}{|\vec{v}_{a2}|} \begin{pmatrix} \cos\phi_a & -\sin\phi_a \\ \sin\phi_a & \cos\phi_a \end{pmatrix} \quad . \tag{21}$$

The application of this ABL scheme implies horizontal homogeneity. Thus, it is implicitly assumed that the boundary layers develop separately over the ice free and the ice covered part of a grid cell. With respect to this the coupling of the ABL model to the SI – OML model is similar to Koch (1988). However, the scheme is extended by the thermodynamic calculations for seven ice-thickness categories in the ice covered part of the grid cell (see section 2). For each of these categories the heat balance is computed with the corresponding ABL quantities. Apart from the surface temperature of ice or snow, respectively, the friction velocity and the stability parameter are determined iteratively, too.

6.2 Results

6.2.1 Preceding experiments

Using the original parameters of both the ABL (Koch, 1988) and the SI – OML model (see section 4), the results of the coupled ABL – SI – OML model were not very promising (see Stössel, 1991, Fig.2). Specifically, the ice extent was significantly reduced compared to the standard results of the SI – OML model. Additionally, the ice-thickness distribution showed a more or less zonal pattern, which could be attributed to a severe underestimation of the ice velocities in the compact ice field.

It was shown in Stössel (1991) that the results could be improved by reducing the model physics of the SI – OML model to

the sea-ice model version of Hibler and Ackley (1983), i.e. by neglecting snow, by using a fixed mixed-layer depth (with constant vertical oceanic heat flux) and by employing a higher lead-closing parameter (h_0; see SLO, section 4.2.4).

Nevertheless, the ice-thickness distribution remained unrealistic, unless the lowermost (1000 hPa) wind field was used to drive the sea-ice model mechanically. This was identified to be due to the naturally weakened orographic impacts on the 850 hPa wind fields as compared to the 1000 hPa ones. Thus, for the following experiments, the use of the higher-level winds has been withdrawn, thereby reducing the higher-level forcing to the temperature and humidity fields only.

6.2.2 Sensitivity to roughness length

Retaining the formalism of the ABL model and the ABL – SI – OML coupling scheme as described above, there are two possibilities to improve the results. According to Koch (1988), the roughness length over ice was specified by $z_{si} = 2 \cdot 10^{-4}$m. This is twice the value for ice free water surfaces ($z_{so} = 1 \cdot 10^{-4}$m) and is usually taken as the local roughness length for smooth ice surfaces (Hanssen-Bauer and Gjessing, 1988; Claussen, 1991), i.e. based on the assumption that the ice field is 100% compact and no surface structures are present (skin drag). This, however, is not consistent with observations in the pack ice of the Southern Ocean. Instead, ice free areas in form of leads are on large-scale nearly always present even within a compact ice field. Specifically, a pack-ice field is generally not characterized by a homogeneous slab, but consists of consolidated floes of different size and freeboard. Additionally, in compact ice areas pressure ridges are expected to form under compressions (Wadhams et al., 1987). In order to achieve the total stress under consideration of those surface structures, it appears feasible to add a so called form drag to the skin drag mentioned above (Arya, 1975). For the present large-scale simulation it seems to be adequate to employ the combined drag for the entire ice field, which corresponds to an increase of the roughness length over ice by 2 orders of magnitude (Hanssen-Bauer and Gjessing, 1988).

The kinetic energy input into the mixed layer is calculated via

the ice velocity, which in grid cells without ice is determined with zero ice mass. This velocity is primarily provided by the air drag, which in the present case with ABL coupling is determined by the stability-dependent friction velocity. When a grid cell is ice free, the friction velocity depends on the roughness over open water (z_{so}). In order to achieve energetical consistency with the kinetic energy input of the SI - OML model without boundary-layer algorithms (where the drag over ice and water was the same), z_{so} is also raised by 2 orders of magnitude. It is noticed that this specification differs from the corresponding one in section 5.

The effect of this measure on the ice-thickness distribution is shown in Fig. 14. Although this experiment yields a substantial improvement compared to the result achieved with the smaller roughness lengths, the characteristic ice-thickness distribution is still missing (as can be seen when comparing Fig. 14 with Fig. 2 and 8). Instead, the rather zonal ice-thickness distribution indicates that the higher roughness length over ice hardly has any impact on the locally computed friction velocity.

This feature becomes obvious in a further experiment where the roughness length over open water is reset to the original (lower) value. In this experiment, the result is nearly unchanged compared to the control run, where both z_{si} and z_{so} have the lower values. In other words: the improvement of the results is primarily due to the increased roughness length over open water. Since the "imaginary" ice velocity calculated with the higher roughness length is only slightly larger, the more realistic result is attributed to higher turbulent heat fluxes, which over ice free water lead to stronger cooling and higher growth rates of new ice.

With respect to the application of the ASL parameterization (section 5), the reduced summer mixed-layer depth shown in Fig. 12.a as compared to Fig. 5.a is to a great extent related to the fact that in an ice free grid cell the turbulent kinetic energy transfer is determined via a z_{so}, which itself is dependent on the Charnock constant and the instantaneous friction velocity. This yields a roughness length which is generally 2 to 3 orders of magnitude lower than the specified value of $z_{si} = 1 \cdot 10^{-3}$m. Larger mixed-layer depths and correspondingly higher (and more realistic) oceanic heat fluxes can thus be achieved by adjusting the

determination of the turbulent kinetic energy input (e.g. via z_{so}).

In section 4, where the turbulent kinetic energy input into the mixed layer is dependent on a constant drag coefficient (C_{da} = $2.7 \cdot 10^{-3}$, which is equal for the ice covered and open water part), the larger mixed-layer depth is primarily due to the higher (real and imaginary) ice drift (over divergent ice covered regions and ice free regions). On the other hand, an enhanced cooling of the mixed layer (as achieved in the previous simulation with both z_{so} and z_{si} raised by 2 orders of magnitude) was not induced, because the change of the drag coefficient has no influence on the calculation of the turbulent heat fluxes (which are rather dependent on the so called transfer coefficients).

6.2.3 Ratio of drag coefficients

Another sensitive parameter in the coupled ABL – SI – OML model is the oceanic drag coefficient, C_{do}. According to McPhee (1980), the proper choice of this parameter is determined less by its absolute value. Instead, it depends more on its ratio to the corresponding coefficient between ice and atmosphere, C_{da} (see section 4). The value for this ratio varies between 2.0 and 1.4 depending on author and region (McPhee, 1980; Leppäranta, 1981; Hoeber and Gube-Lehnhardt, 1987). Since in the ABL model C_{da} is calculated via u_* ($C_{da} = u_*^2/|\vec{V}_{a2}|^2$), this coefficient becomes a diagnostic variable. Thus, C_{do} should accordingly also be treated as a variable in order to keep the ratio of the two coefficients fixed. Such an experiment, however, yielded unrealistic results in the form of an overestimation of the drift rates in the divergent field. This is due to the fact that the friction effect of the ocean on the ice (generally in form of a negative acceleration) becomes negligible below a critical value of the air drag (generally during strong stable stratification in the ABL). A reduction of C_{do}, e.g. to half the original value, on the other hand, yields much more realistic results (not shown).

6.2.4 Influence of wind turning

A variable in the ABL model which is dependent on the roughness length or the friction velocity, respectively, is the turning

angle of the wind in the Ekman layer. Suppose z_{si} = 0.001 m (as specified in the AGC model of the ECMWF) is underestimated, giving rise to increase z_{si} by one order of magnitude, differences in the turning angle of up to 15° occur with the present ABL – SI – OML model. For the Antarctic region, similar studies were conducted by Mitchell and Senior (1989) with the AGC model of the United Kingdom Meteorological Office (UKMO). The motivation for their study was the investigation of the sensitivity of the AGC model to different ice extents. They reduced the large-scale surface roughness over ice covered regions by 3 orders of magnitude and examined this effect separately from the other influences of sea ice (surface temperature, albedo, etc.). In the lower layers of the higher latitudes this measure yielded a reduction of the turning from the circumpolar westwinds to higher latitudes, where it induced a lowering of the surface pressure. To inversely investigate the impact of this effect on the ice, the 1000 hPa winds are treated as geostrophic winds with respect to the wind turning in the following experiment (Fig. 15). This can be justified by the assumption that the lower-level winds in the AGC model are turned too weakly due to the presumably underestimated roughness length over ice. Otherwise, the experiment is analogous to the previous one (Fig. 14). In the results of the new experiment, the strong ridging at Mawson (60°E) and off Victoria Land is reduced. In summer, a distinct ice tongue is apparent in the eastern Ross Sea; in winter, the thinner ice off the Ross ice shelf is shifted more to the west because of the higher convergence in the cyclonic gyre, whereas the thicker ice off Marie Byrd Land is more pronounced. In comparison to the previous run, these alterations are a significant improvement towards observations (see Fig. 10.a; Jacobs and Comiso, 1989).

Analyzing this experiment, it must be mentioned that the effect of the wind turning is on the one hand certainly overestimated, since an increase of the roughness length by one order of magnitude yields at most half of the presently achieved turning angle. On the other hand, the wind turning is not very effective over compact ice because of the high static stability in the ABL. In the MIZ, though, it can be assumed that the roughness is much higher due to the lower ice concentration (Andreas et al., 1984;

Mitchell and Senior, 1989). There, the wind turning in the AGC model based on $z_{si} = 0.001$ m is expected to be severly underestimated. This is especially true in spring and summer (comp. Figs.9.a and 9.d or Figs.10.a and 10.d, respectively), when the ice concentration is generally lower. Additionally, the stratification of the ABL becomes less stable in summer, thus increasing the strength of the coupling between atmosphere and sea ice. This leads to a higher effectiveness of the additional wind turning and to the improved results.

6.2.5 Increase of buoyancy fluxes

So far it was assumed that the dynamic forcing of the oceanic mixed layer and of the sea ice, respectively, is dependent on the separately calculated local friction velocity (and thus on the local stability). Furthermore, from the seven ice-thickness categories of the ice covered part of a grid cell, the friction velocity calculated using the fourth category (k = 4 in (8), corresponding to the effective ice thickness $\tilde{h}_i$ (see (3))) was used to derive the stress over ice. Assuming (realistically) that the (pack-) ice field consists of floes of different size and that ice free areas are homogeneously distributed all over a grid cell, it certainly makes more sense to employ one ice-concentration weighted friction velocity for the entire grid cell instead of the locally calculated ones. A correspondent experiment, however, was not very successful. Although the ice became more mobile in the MIZ, the effect of the modification was negligible in the major part of the pack-ice area, which (at least in the simulation) is rather compact ($95\% < N_i \leq 100\%$).

It has to be emphasized, however, that the destabilizing influence of leads on the stratification of the ABL is generally non-linearly weighted with the ice concentration. It is rather dependent on the width of the leads. In particular, the turbulent heat fluxes are inversely proportional to the downwind fetch over a lead. Thus, the local turbulent heat exchange is more effective, the smaller the lead width is (Worby and Allison, 1991). Since the present sea-ice model does not contain any information about floe sizes or lead widths, these ought to be specified in order to determine the downwind fetch. Since this would be rather

arbitrary, no such attempt has been made here.

A more realistic result can e.g. be achieved by (exaggeratedly) employing the drag calculated over the ice free part for the mechanical forcing of the sea ice (Fig.16). This experiment clearly yields the characteristic ice-thickness distribution, which, as expected, generally overestimates ice ridging (compare with Figs.2 and 8). This means that the appropriate magnitude of stress between atmosphere and sea ice for the ABL – SI – OML model is placed somewhere in between both extreme cases shown above.

In Fig.17 the seasonal cycles of ice extent and effective ice area (defined as $\Sigma(A_{gr} \cdot N_i)$, where A_{gr} is the grid cell area) from the current sensitivity simulation (thick lines) are shown in comparison to the corresponding cycles for the year 1986 derived from Scanning Multichannel Microwave Radiometer (SMMR) data (thin curves) (Gloersen and Campbell, 1988). The minimum ice extent is about $1 \cdot 10^6 km^2$, which is about $2 \cdot 10^6 km^2$ smaller than observed, while the maximum ice extent is about $18 \cdot 10^6 km^2$ and thus rather close to the observed maximum. With respect to the effective ice area, too, the simulated maximum for 1986 (ca. $15.8 \cdot 10^6 km^2$) is rather close to the observations ($15.0 \cdot 10^6 km^2$), while the corresponding value with surface forcing (section 4) is overestimated by about $2.5 \cdot 10^6 km^2$.

6.2.6 Interannual variation

In particular, it was not possible to simulate the interannual variation between 1985 and 1986 when the atmospheric thermal forcing was derived from the lower (1000 hPa) level of the global analyses. Figs.18 and 19 present the simulated (thick curves) and the SMMR-data derived (thin curves) seasonal cycles of the ice extent for 1985 (dashed curves) and 1986 (full curves).

The simulation results in Fig.18 are from the ASL – SI – OML model (section 5), while those in Fig.19 are from the ABL – SI – OML model including enhanced buoyancy fluxes (according to section 6.2.5) and additional wind turning (according to section 6.2.4). The latter supplement refers to the fact that the summer ice extent in the Ross Sea is more realistic with additional wind turning (Fig.15) and thus more distinctly resolved with respect to the interannual variability. A comparison with

Fig. 17 shows that this modification has a major impact only on the summer ice extent.

Comparing the results of the latter experiment to the seasonal cycles derived from the SMMR data (Fig. 19), it is obvious that the transient simulations with the thermal forcing from the 850 hPa level represent the relative variation between both years much more realistically than with the corresponding 1000 hPa forcing (Fig. 18). With respect to the winter maximum even the absolute value is about correct.

The main reason for the failure with thermal forcing from near-surface is certainly due to the fact that these variables are too closely related to the specified lower boundary conditions of the AGC model. Since the year 1986 was rather anomalous in the sense that the winter maximum ice extent was far below the climatological value (Gloersen and Campbell, 1988), the described climatological treatment of the MIZ in the AGC model (see section 4) yielded colder than observed temperatures in the lowest level of the AGC model and thus the discrepancy in maximum ice extent between the observation and the simulation shown in Fig. 18.

The larger ice extent in the winter season 1986 compared to 1985 (Fig. 18) is presumably attributed to differences in the large-scale circulation of the two years, since similar fluctuations can be identified in Fig. 19 (the wind forcing field is identical in both cases).

Investigating the interannual variability with the presently used global analyses of the ECMWF, attention must be drawn to the fact that occasionally alterations were introduced in the analyses and model schemes of the forecast model (Trenberth and Olson, 1988). These may induce significant changes in the results (e.g. due to the increase of the horizontal resolution (T-106 on May 1st 1985) or due to the introduction of the gravity wave drag (on July 15th 1986))(Bengtsson and Shukla, 1988).

7. Discussion

The results presented in the last section showed that under certain conditions, improvements can be achieved in the simulation of the seasonal cycle of ice extent, the areal distribution of ice

thickness and the interannual variation when ABL effects are considered.

Concerning the mechanical forcing of the ABL – SI – OML model the most important of these conditions is the substitution of the 850 hPa wind field by the 1000 hPa wind field. The reason is the fact that orographic features are hardly detectable in the upper wind field. These are, however, crucial in reproducing local sea-ice characteristics along the coast of Antarctica realistically, especially east of the Peninsula and off Victoria Land (Schwerdtfeger, 1979). Even in the 1000 hPa wind field of the global analyses local wind features like katabatic and barrier winds are often underestimated.

Another crucial point for the coupling of atmosphere, sea ice and ocean is the parameterization of the surface roughness. This is specifically important for the calculation of the turbulent heat fluxes and the turbulent kinetic energy input into the ice free part of the OML (which without ASL or ABL coupling was determined via a constant transfer and drag coefficient), implying a proper adjustment e.g. via the roughness length.

With additional wind turning, the results improved within the ice edge area in summer indicating that the lower boundary conditions in the AGC model might be inadequately specified in that specific area. This is an example of an inconsistency which may occur when forcing fields are employed which are primarily model generated.

A more realistic ice-thickness distribution can be achieved after a drastic increase of the buoyancy fluxes. Since an ice-concentration weighted determination of the surface stress was not very effective, it can be inferred that the ABL model decouples the atmosphere from the sea ice too strongly. This feature, specifically occuring over sea ice, is also observed with other one-dimensional ABL models (Louis, 1979). As was shown in the previous simulations with reduced model physics (Stössel, 1991), snow cover, too, is a crucial factor with respect to this problem, since it isolates the atmosphere from the ocean more strongly than sea ice alone.

Comparing the results of section 6 with those of sections 4 and 5, the generally underestimated ice extent in the Weddell Sea is

striking. It occurs even when additional barrier wind effects are included (additional wind stress specified at the grid cells next to the Peninsula; results not shown) and with additional wind turning (Fig.15). This feature can be explained as follows: the Weddell Sea with the Peninsula in the west extending far to the north, represents an anomaly with respect to the coastal topography as well as to the orography, as compared to the major geographic structure of the Antarctic continent. The anomalous structure favours on average the formation of cyclonic currents and winds which are locally supported by katabatic winds in the south-east and barrier winds in the west. Due to this forcing and the shelter at the west flank, the ice drifts far to the north until it is captured by the west-wind drift, driving it further east-north-east. This anomaly of the sea-ice extent naturally affects the adjacent spheres, ocean and atmosphere. This can be found e.g. from a difference plot of the potential temperature between the 1000 hPa level and the 850 hPa level of the global analyses of the ECMWF (Fig.20). There is a pronounced seasonal variation in the temperature difference between the two layers. As can be expected, the temperature difference is largest over ice (inversion). The anomaly over the Weddell Sea is striking, with large gradients extending up to 60°S.

In spite of the fact that the stability in the ABL model adjusts to the specific situation at the surface, which practically means that the warmer air of the 850 hPa layer is effectively decoupled from the sea ice, the pure vertical description of the ABL appears to be insufficient in this case. Instead, advective processes seem to dominate. Specifically, cold-air advects into the western and northern parts of the Weddell Sea below the inversion. A compensating warm-air advection from the west-wind zone into higher latitudes exists at higher levels (Schwerdtfeger, 1984). These advection processes are mainly responsible for the extreme vertical temperature gradients observed over major parts of the Weddell Sea (Fig.20). Due to the missing three-dimensionality, these gradients cannot be captured by the present ABL model. This finally leads to an underestimation of the ice thickness and ice extent in the Weddell Sea.

Analogous features are to be expected in the ocean, where the

situation is complicated by the northward transport of fresh water at the surface (ice drift + ice melt) and by the topography of the continental shelf. Specifically, advection of warmer water onto the shelf region may occur. This is induced by upwelling processes at the continental slope, which compensate the sinking of colder and more saline water produced over the shelf primarily by new-ice formation. This is especially observed over the continental shelf of the Ross Sea, where the ice concentration in winter is generally lower than over the deep sea (Jacobs and Comiso, 1989).

8. Conclusions and requirements

Except for the interannual variation, the most realistic results were achieved with the ASL – SI – OML model. This is important primarily for sea-ice forecasts, whose quality, of course, will be mainly dependent on the quality of the weather forecasts. For long-time integrations the negative impact of the specified boundary conditions in the AGC model can be reduced by determining these in near real-time (similar to the SST) instead of the employing climatological values. The surface temperature could e.g. be determined as a function of the real-time, satellite-derived ice concentration.

With regard to the inconsistencies which might occur when model derived forcing fields are employed (section 7), it is noticed that the severity of such problems depends, of course, on the quality of the model where the forcing fields are derived from, on the quality of its lower boundary conditions and on the computations used from that model. At locations where inconsistencies arise, a careful analysis is required by means of adjusting the unknown parameters of both the model which generates the forcing fields, and the model which is forced. This could be realised in an iterative procedure. The results may subsequently be used for coupled experiments.

Evaluating the present results it must be emphasized that the Southern Ocean region is probably the most difficult one to simulate. This is due less to the physical description of sea ice in the models. Instead, the atmospheric forcing data seem to be the most crucial component in the modelling attempts. In view of

this deficiency the presently achieved results appear to be promising.

The results of this paper stress the strong interactions between sea ice and the adjacent boundary layers. This is especially important for the projected coupled AGC – SI – OGC model. An important question is the integrated effect of the energy transfer between atmosphere and ocean. The energy fluxes averaged over one model grid cell should be determined as function of the local ice compactness and the ice thickness of the ice covered part of that grid cell. This can only be achieved by incorporating the boundary-layer processes, which adjust interactively to current variations in sea-ice conditions.

Another crucial point is the deficit of mass, energy and momentum at the atmosphere-ocean interface which is temporarily stored in sea ice. Depending on the instantaneous ambient physical conditions this requires an accurate determination, which can only be guaranteed if the energy transfer between atmosphere and ocean is consistent with the comprehensive physics of the sea ice. In this sense, it is equivalently important for the energy and fresh water stored in sea ice (e.g. in form of ice thickness) to be advected in accordance with proper sea-ice dynamics, especially under consideration of rheological properties. This is specifically important for an OGC model, where higher salinity occurs in areas of thermodynamic sea-ice growth (and consequent deep convection). This sea ice is advected (presumably accompanied by ridging and rafting processes) and subsequently melted far remote from the location of ice formation, inducing a freshening of the ocean surface layer (and thus a stable stratification).

If these sea-ice related physical processes are not definitely considered in the coupling of atmosphere and ocean on GCM scales, unrealistic results are to be expected for long-time integrations. Then, the discrepancies to observed patterns can only be avoided by crude unphysical measures (e.g. by the so called "flux correction" or "flux anomaly coupling"; Sausen et al., 1988).

Thus, the polar regions, where the ocean surface appears in a frozen stage, provide a unique environment for the verification of coupled atmosphere – ocean models, sea ice being the sensitive control variable for the skill of the simulations in terms of a

proper exchange of energy, mass and momentum. Finally, errors due to neglection of sea-ice physics in AGC – SI – OGC models are not restricted to the specific sea-ice regions and their boundary layers, but may extend over a global scale (Meehl and Washington, 1990), e.g. via an unrealistic simulation of the deep-water production.

Notation:

Symbols:

A : area

c : specific heat capacity

C : coefficient

f : Coriolis force

F : net fresh-water flux

F′ : stability function

$\vec{F}$: force due to internal ice stress

g : acceleration due to gravity

h : thickness

H : sea level due to dynamic topography

k : thermal conductivity

L : specific latent heat

L′ : Monin-Obukhov length

N : coverage

p : pressure

P : precipitation rate

P^* : ice strength parameter

q : specific humidity

Q : heat flux density

$\tilde{Q}$: heat flux

Ri : Richardson number

S : salinity

$\tilde{S}$: salt flux

T : temperature

u_* : friction (scaling) velocity

w : vertical (z → upward) velocity component

$\vec{V}$: horizontal velocity

z_s : roughness length

α : albedo

δ' : turbulent length scale

ε : emissivity

θ : potential temperature

θ_* : scaling temperature

κ : von Karman constant

μ : stability parameter

ρ : density

σ : Stefan-Boltzmann constant

σ_{kl} : stress tensor

$\vec{\tau}$: surface stress

ϕ : turning angle

φ : latitude

Indices:

a : atmosphere

b : bottom (interface ice/sea water)

c : conductive

cl : cloud

d : drag

e : entrainment

f : fusion

g : geostrophic

gr : grid cell

h : turbulent heat flux

Hc : halocline

i : ice

la : latent heat

lw : longwave radiation

m : momentum flux

o : ocean

s : surface

se : sensible heat

sn : snow

sw : shortwave radiation

Tc : thermocline

v : vaporization

w : water

1 : first neighboring layer to surface

2 : second neighboring layer to surface

Acknowledgements:

Thanks are due to P.Lemke, M.Heimann, K.Herterich, C.Koch, P.Loewe and E.Roeckner for valuable discussions and advice during this study, to L.Bengtsson and P.Lemke for reviewing the manuscript, to W.D.Hibler, W.B.Owens, and again C.Koch and P.Lemke for providing their models, to M.Grunert for finishing the drafts, to P.Besemann for reviewing the manuscript with regard to English language, to the Deutscher Wetterdienst (DWD), Offenbach, for delivering the global analyses of the ECMWF, and to R.Schnur for preprocessing these data. This work was supported by the Sonderforschungsbereich (SFB) 318.

References

Andreas, E. L., W. B. Tucker and S. F. Ackley (1984): Atmospheric boundary-layer modification, drag coefficient, and surface heat flux in the Antarctic marginal ice zone. *J. Geophys. Res., 89 (C1), 649-661.*

Arya, S. P. S. (1975): A drag partition theory for determining the large-scale roughness parameter and wind stress on the Arctic pack ice. *J. Geophys. Res., 80, 3447 - 3454.*

Bengtsson, L. and J. Shukla (1988): Integration of space and in situ observations to study global climate change. *Bull. American Meteor. Soc., 69 (10), 1130 - 1143.*

Bryan, K. (1969): A numerical method for the study of the circulation of the World Ocean. *J. Comp. Phys., 4, 347 - 376.*

Businger, J. A., J.C. Wyngaard, Y. Izumi and E.F. Bradley (1971): Flux profile relationships in the atmospheric surface layer. *J. Atm. Sci. , 28, 181-189.*

Cattle, H. und D. L. Roberts (1988): The performance of atmospheric circulation models in polar regions. In: *Rep. of the third session of the Working Group on Sea Ice and Climate, Oslo,WCRP-18, WMO/TD-No. 272, Annex A.*

Claussen, M. (1991): Local advection processes in the surface layer of the marginal ice zone. *Bound. Layer Met., 54, 1 - 27.*

ECMWF Research Department (1985): Research manual 3, ECMWF forecast model, physical parameterisation. *ECMWF Met. Bull., M 1.6/2 (1), Rev. 1.*

ECMWF Research Department (1986): Research manual 1, ECMWF data assimilation, scientific documentation. Eds.: *P. Lönnberg and D. Shaw, ECMWF Met. Bull., M 1.5/1 (1), Rev. 1.*

Fiedler, F. and H.A. Panofsky (1972): The geostrophic drag coefficient and the effective roughness length. *Quart. J. Roy. Met. Soc., 98, 213-220.*

Foreman, S. J., N. S. Grahame, K. Maskell and D. L. Roberts (1988): Feedbacks and error mechanisms in a global coupled ocean/atmosphere/sea-ice model. In: *Modelling the Sensitivity and Variations of the Ocean-Atmosphere System, Rep. of a workshop at the ECMWF, Reading WCRP-15, WMO/TD-No. 254, 271-279.*

Gloersen, P., and W. J. Campbell (1988): Variations in the Arctic, Antarctic and global sea ice covers during 1978 - 1987 as observed with the Nimbus 7 Scanning Multichannel Microwave Radiometer. *J. Geophys. Res., 93 (C9), 10666 - 10674.*

Gordon, A. L. and B. A. Huber (1990): Southern Ocean winter mixed layer. *J. Geophys. Res., 95 (C7), 11655 - 22672.*

Hanssen-Bauer, I. and Y. T. Gjessing (1988): Observations and model calculations of aerodynamic drag on sea ice in the Fram strait. *Tellus, 40 A, 151 - 161.*

Heimann, M. and P. Monfray (1991): Spatial and temporal variation of the gas exchange coefficient for CO_2: 1. data analysis and global validation. *J. Geophys. Res., in press.*

Hibler, W. D., III (1979): A dynamic thermodynamic sea ice model. *J. Phys. Oceanogr., 9, 815 - 846.*

Hibler, W. D., III (1984): The role of sea ice dynamics in modeling CO_2 increases.In: *Climate Processes and Climate Sensitivity*, eds.: J. Hansen and T. Takahashi, *Geophys. Monogr., 29, 238 - 253.*

Hibler, W. D. III and S. F. Ackley (1983): Numerical simulation of the Weddell Sea pack ice. *J. Geophys. Res., 88, 2873 - 2887.*

Hoeber, H. and M. Gube-Lehnhardt (1987): The eastern Weddell Sea drifting buoy data set of the Winter Weddell Sea Project (WWSP). *AWI f. Polarforschung, Bremerhaven, Ber. zur Polarforschung, 37.*

Jacobs, S. S. and J. C. Comiso (1989): Sea ice and oceanic processes on the Ross Sea continental shelf. *J. Geophys. Res., 94 (C12), 18195 - 18211.*

Jaeger, L (1976): Monatskarten des Niederschlags für die ganze Erde. *Berichte des Deutschen Wetterdienstes, 139.*

Janssen, P. A. E. M., P. Lionello, M. Reistad and A. Hollingsworth (1989): Hindcasts and data assimilation studies with the WAM model during the Seasat period. *J. Geophys. Res., 94 (C1), 973 - 993.*

Koch, C. (1988): A coupled sea ice - atmospheric boundary layer model part I: description of the model and 1979 standard run. *Beitr.Phys. Atmosph., 61 (4), 344 - 354.*

Lemke, P. (1987): A coupled one-dimensional sea ice - ocean model. *J. Geophys. Res., 92, 13164 - 13172.*

Lemke, P., E. W. Trinkl and K. Hasselmann (1980): Stochastic dynamic analysis of polar sea ice variability. *J. Phys. Oceanogr., 10, 2100 - 2120.*

Lemke, P., W. B. Owens and W. D. Hibler III (1990): A coupled sea ice - mixed layer - pycnocline model for the Weddell Sea. *J. Geophys. Res.,95 (C6), 9513-9525.*

Leppäranta, M. (1981): On the structure and mechanics of pack ice in the Bothnian Bay. *Inst. f. Marine Res., Helsinki, Finnish Marine Res., 248, 3 - 86.*

Leppäranta, M. and W. D. Hibler III (1985): The role of plastic ice interaction in marginal ice zone dynamics. *J. Geophys. Res., 90 (C11), 11899-11909.*

Louis, J .- F. (1979): A parametric model of vertical eddy fluxes in the atmosphere. *Bound. Layer Met., 17, 187 - 202.*

Maier-Reimer, E. and U. Mikolajewicz (1989): Experiments with an OGCM on the cause of the Younger Dryas. *In: Oceanography 1988, ed.: A. Ayala-Castañares, W. Wooster und A. Yáñez-Arancibia. UNAM Press, México DF, XXXp, 87-100.*

Manabe, S., K. Bryan and M. J. Spelman (1990): Transient response of a global ocean-atmosphere model to a doubling of atmospheric carbon dioxide. *J. Phys. Oceanogr., 20, 722 - 749.*

Martinson, D. G. (1990): Evolution of the Southern Ocean winter mixed layer and sea ice: open ocean deepwater formation and ventilation. *J. Geophys. Res., 95 (C7), 11641 - 11654.*

Maykut, G. A. (1982): Large-scale heat exchange and ice production in the central Arctic. *J. Geophys. Res., 87 (C10), 7971-7984.*

McPhee, M. G. (1980): An analysis of pack ice drift in summer. In: *Sea ice processes and models, ed.: R. S. Pritchard, University of Washington Press, Seattle, 62 - 75.*

Meehl, G. A. and W. M. Washington (1990): CO_2 climate sensitivity and snow - sea ice albedo parameterization in an atmospheric GCM coupled to a mixed - layer ocean model. *Climate Change, 6, 283 - 306.*

Mitchell, J. F. B. and C. A. Senior (1989): The antarctic winter; simulations with climatological and reduced sea-ice extents. *Quart. J. of the Royal Met. Soc., 115, 225 - 246.*

NAVY/NOAA Joint Ice Center (1986): Antarctic ice charts 1985-1986. *Naval Polar Oceanography Center, Washington, D.C.*

Oberhuber, J. M. (1991): Simulation of the Atlantic circulation with a coupled sea ice - mixed layer - isopycnal general circulation model. *J. Phys. Oceanogr., in press.*

Overland, J. E. (1985): Atmospheric boundary layer structure and drag coefficent over sea ice. *J. Geophys. Res., 90 (C5), 9029 - 9049.*

Owens, W. B. and P. Lemke (1990): Sensitivity studies with a sea ice.- mixed layer - pycnocline model in the Weddell Sea, *J. Geophys. Res., 95 (C6), 9527-9538.*

Parkinson, C. L. and W. M. Washington (1979): A large-scale numerical model of sea ice. J. Geophys. Res., 84, 311 - 337.

Sausen, R., K. Barthel and K. Hasselmann (1988): A flux correction method for removing the climate drift of coupled atmosphere-ocean models. *Clim. Dyn., 2, 145-163.*

Schwerdtfeger, W. (1979): Meteorological aspects of the drift of ice from the Weddell Sea toward the mid-latitude westerlies. *J. Geophys. Res., 84, 6321 - 6328.*

Schwerdtfeger, W. (1984): Weather and Climate of the Antarctic. *Developments in Atmospheric Science 15, Elsevier Publ. Co., Amsterdam.*

Semtner, A. J., Jr. (1974): An oceanic general circulation model with bottom topography. *Numerical Simulation of Weather and Climate, Dept. of Meteorology, Univ. of California, Los Angeles, Tech. Rep. No. 9.*

Semtner, A. J., Jr. (1976): A model for the thermodynamic growth of sea ice in numerical investigations of climate. *J. Phys. Oceanogr., 6, 379-389.*

Stössel, A. (1991): Application of an atmospheric boundary layer model to a large-scale coupled sea ice - oceanic mixed layer model for the Southern Ocean. *Ann. of Glaciology, 15, in press.*

Stössel, A., P. Lemke and W. B. Owens (1990): Coupled sea ice - mixed layer simulations for the Southern Ocean. *J. Geophys. Res., 95 (C6), 9539 - 9555.*

Thorndike, A. S. and R. Colony (1982): Sea ice motion in response to geostrophic winds. *J. Geophys. Res., 87, 5845 - 5852.*

Trenberth, K. E. and J. G. Olson (1988): ECMWF global analyses 1979 - 1986: Circulation statistics and data evaluation. *NCAR, Boulder, Colorado, Tech. Note, TN-300 + STR.*

Trenberth, K. E., J. G. Olson and W. G. Large (1989): A global ocean wind stress climatology based on ECMWF analyses. *NCAR, Boulder, Colorado, Tech. Note, TN-338 + STR.*

van Ypersele, J.- P. (1986): A numerical study of the response of the Southern Ocean and its sea ice to a CO_2 - induced atmospheric warming. *Fac. des Sci., Univ. Cath. de Louvain, Louvain la Neuve, Ph.D. thesis.*

Wadhams, P., M. A. Lange and S. F. Ackley (1987): The ice thickness distribution across the Atlantic sector of the Antarctic Ocean in midwinter. *J. Geophys. Res., 92,(C13), 14535 - 14552.*

Worby, A. P. and I. Allison (1991): Ocean - atmosphere energy exchange over thin, variable concentration Antarctic pack ice. *Ann. of Glaciology, 15, in press.*

Zwally, H. J., J. C. Comiso, C. L. Parkinson, F. D. Carsey, W. J. Campbell and P. Gloersen (1983): Antarctic Sea Ice 1973 - 1976: Satellite Passive - Microwave observations. *NASA, Washington, D.C., SP-459.*

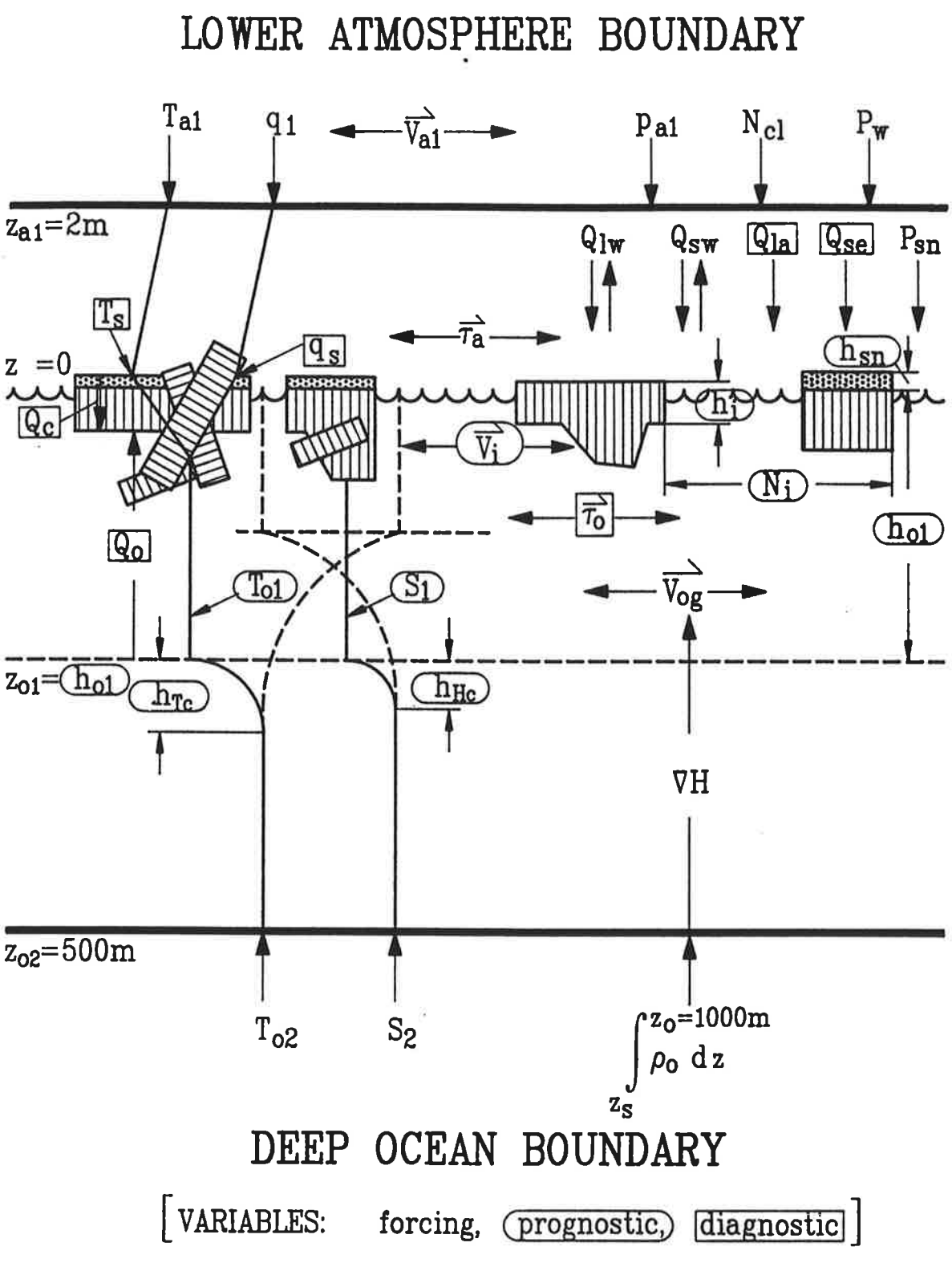

Fig.1: Viewgraph of the variables of the SI – OML model (symbol explanations see notation list).

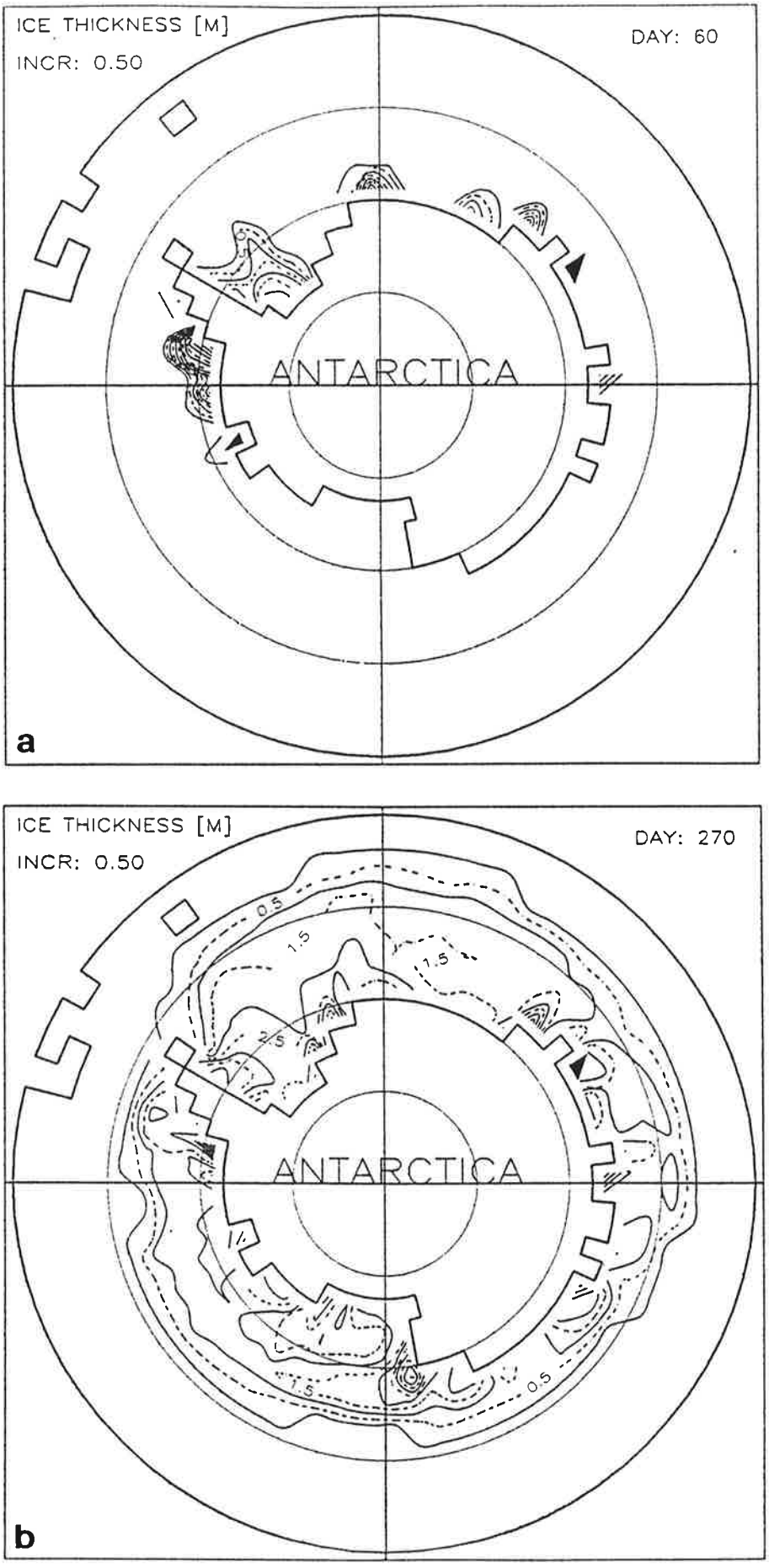

Fig. 2: Ice-thickness contours simulated with the SI – OML model employing a higher ice strength and a larger surface stress, representing the approximate dates of minimum (a: 1.3.1986) and maximum (b: 27.9.1986) ice extent.

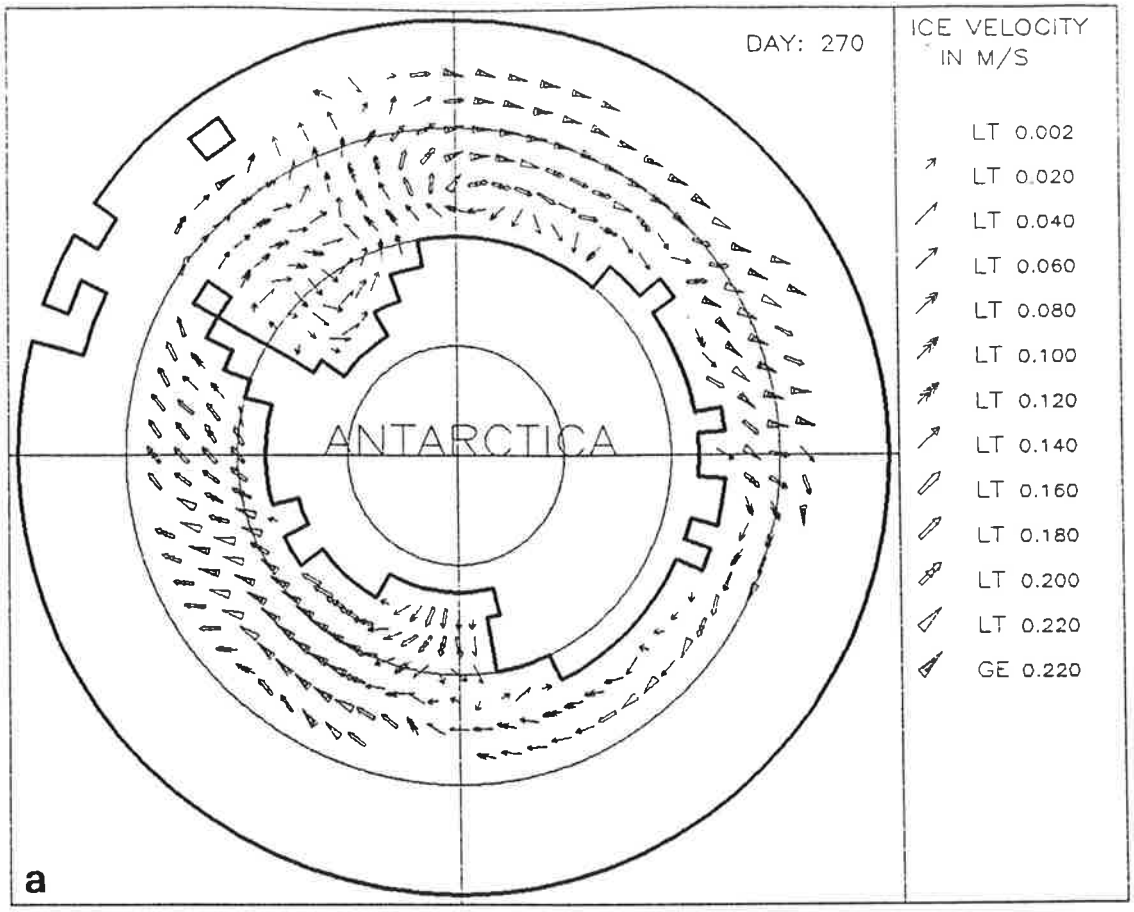

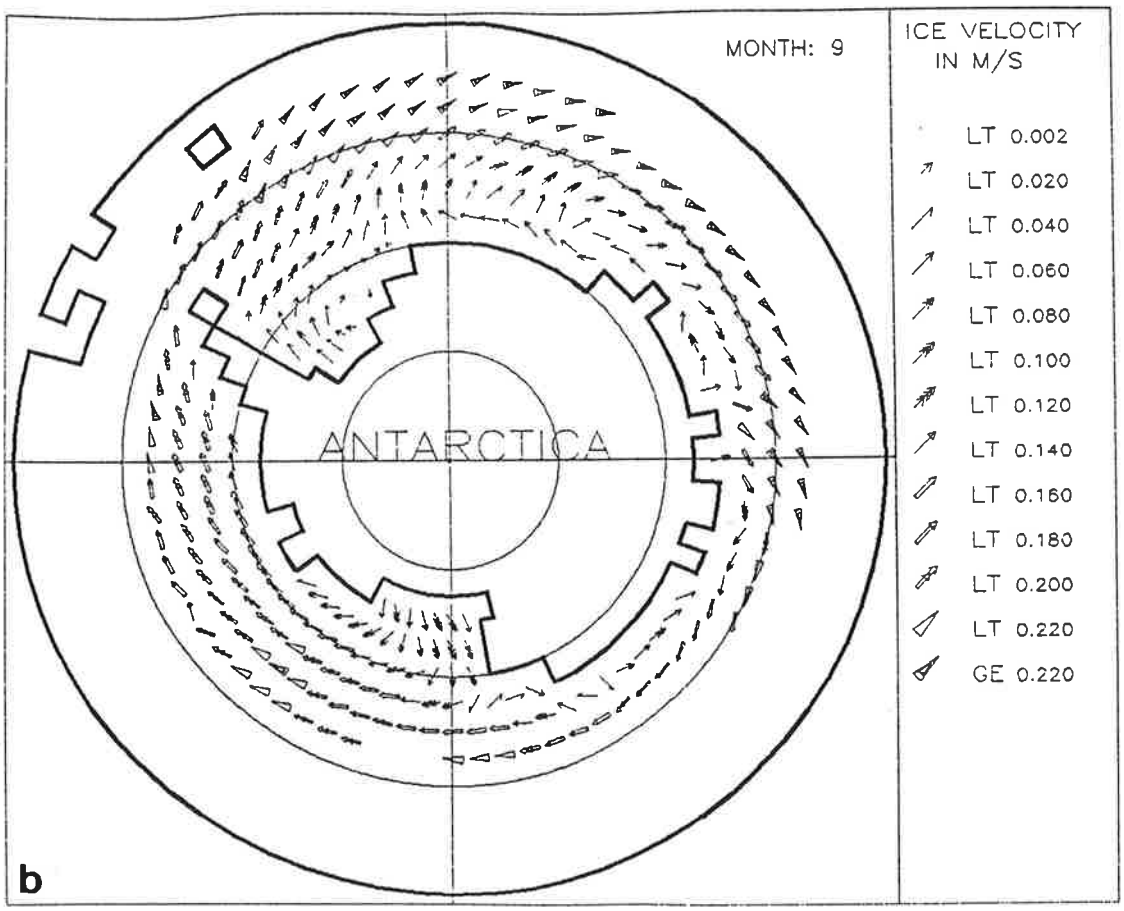

Fig.3: Ice velocities from the same model version as in Fig.2, for the approximate date of maximum ice extent (a: 27.9.1986) and the monthly mean of September 1986 (b).

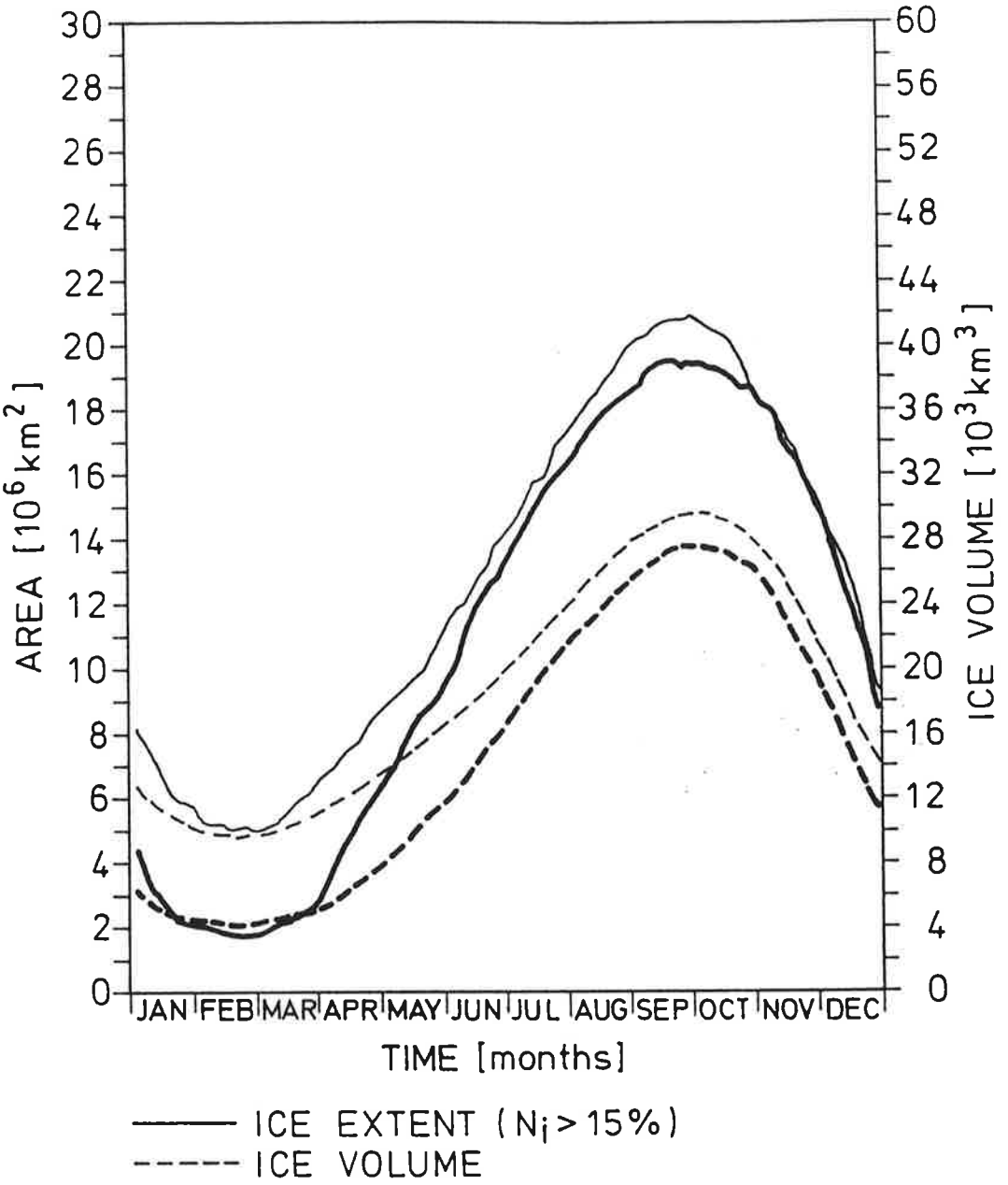

Fig.4: Seasonal cycles of ice extent and ice volume from the same model version as in Fig.2 (thick curves) and from the standard SI – OML model employing climatological monthly mean forcing as presented in SLO (thin curves).

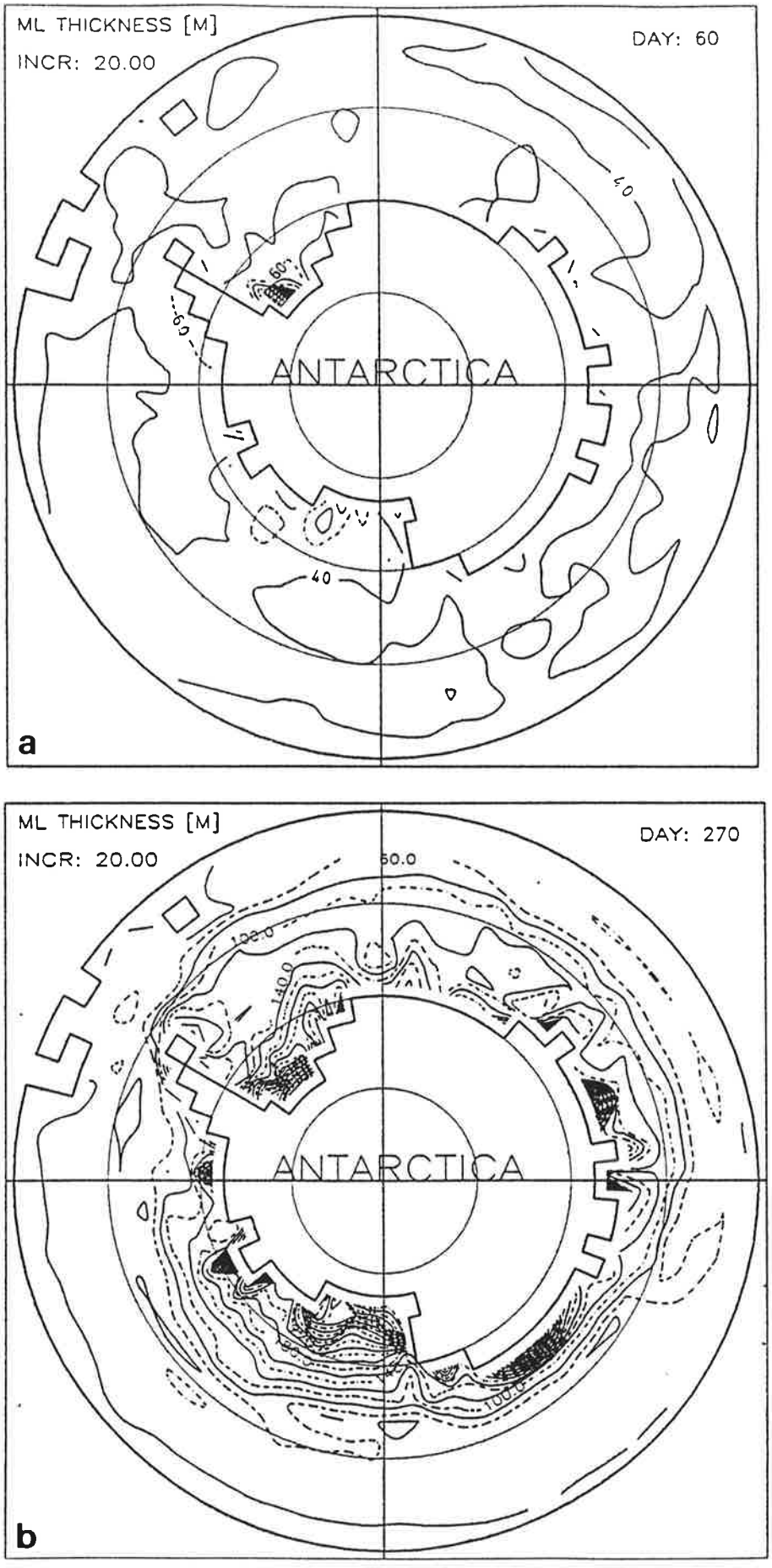

Fig.5: Contours of oceanic mixed-layer depth from the same model version and for the same dates as in Fig.2.

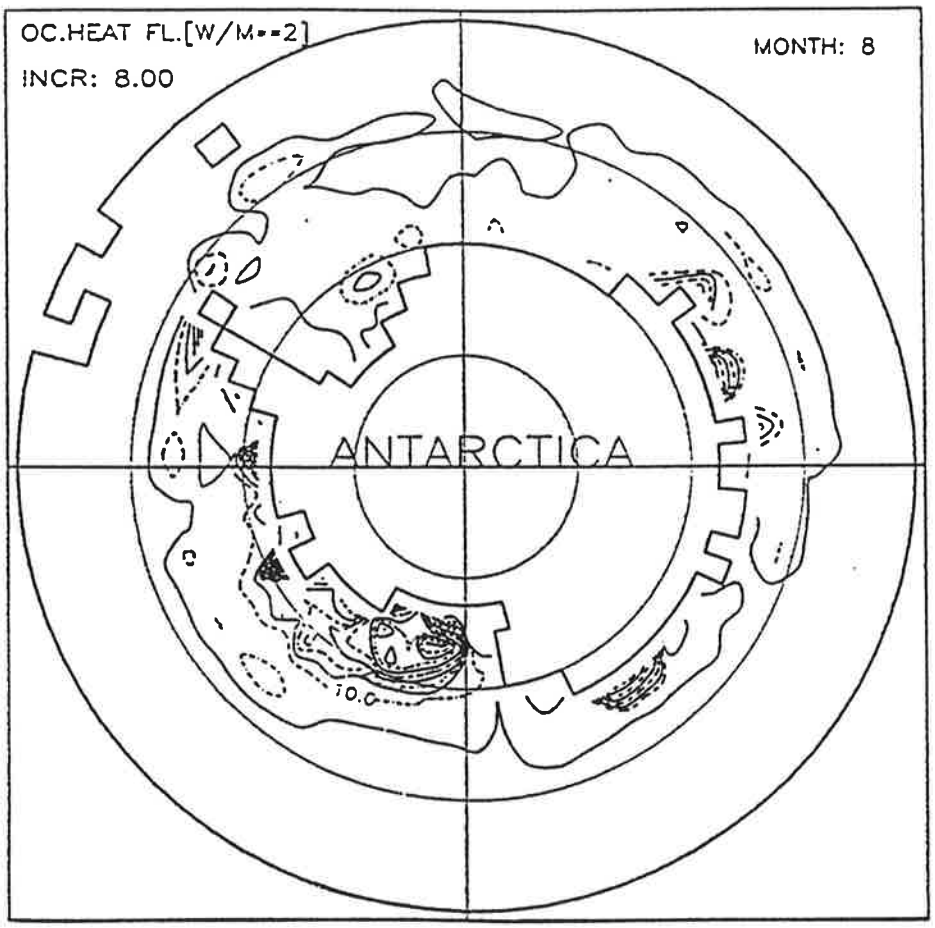

Fig.6: Contours of the monthly mean vertical oceanic heat flux of August 1986 from the same model version as in Fig.2; the minimum contour line represents 2 W/m^2. Note that the increment is 8 W/m^2.

Fig.7: Net freezing rate in equivalent meters of ice thickness for the sixth simulation year of the same model version as in Fig.2. The broken lines (negative) represent more melting than freezing, the thin, full lines the opposite.

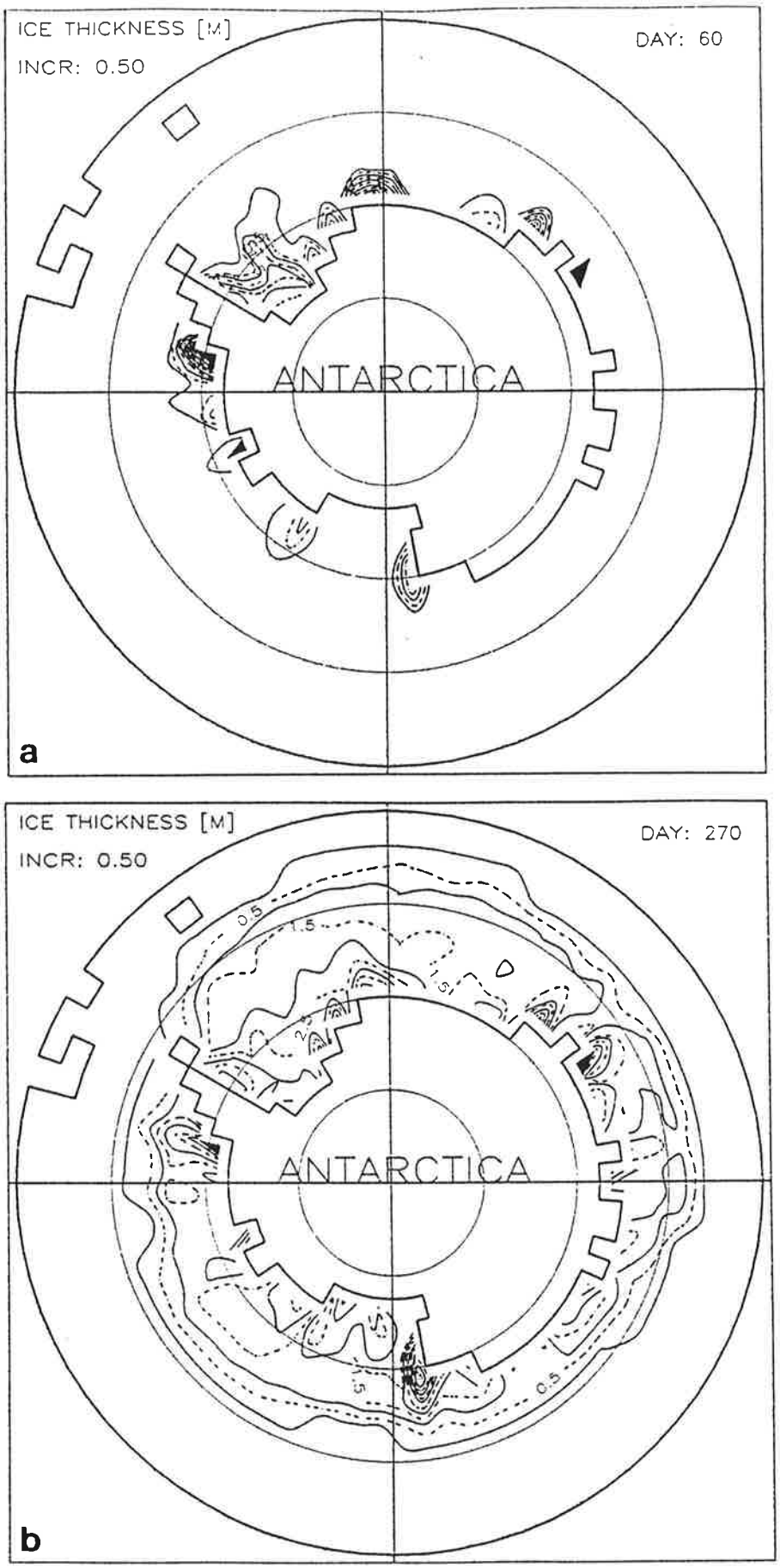

Fig.8: Ice-thickness contours simulated with the ASL – SI – OML model for the same dates as in Fig.2.

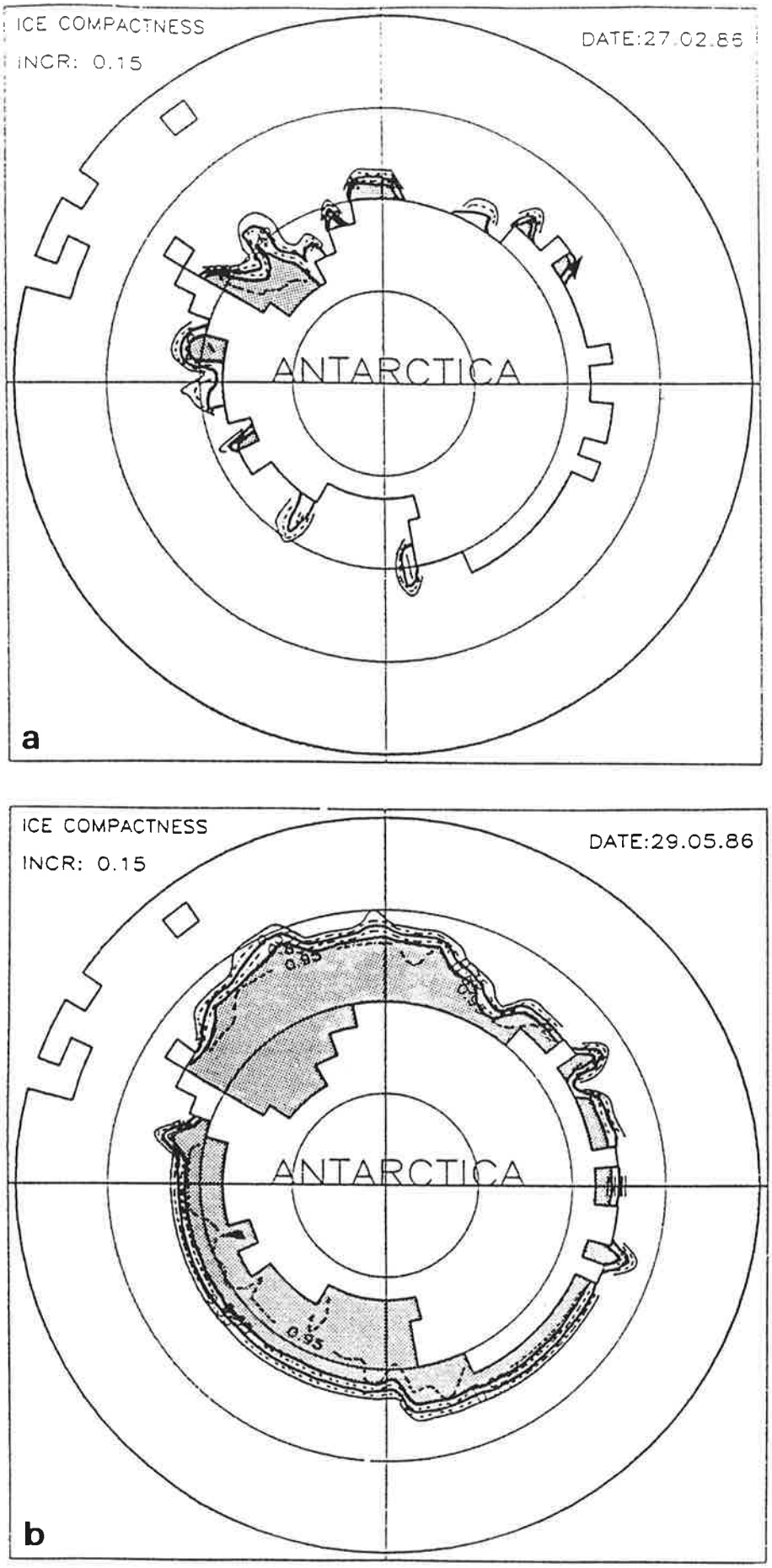

Fig. 9

(Text see page 52)

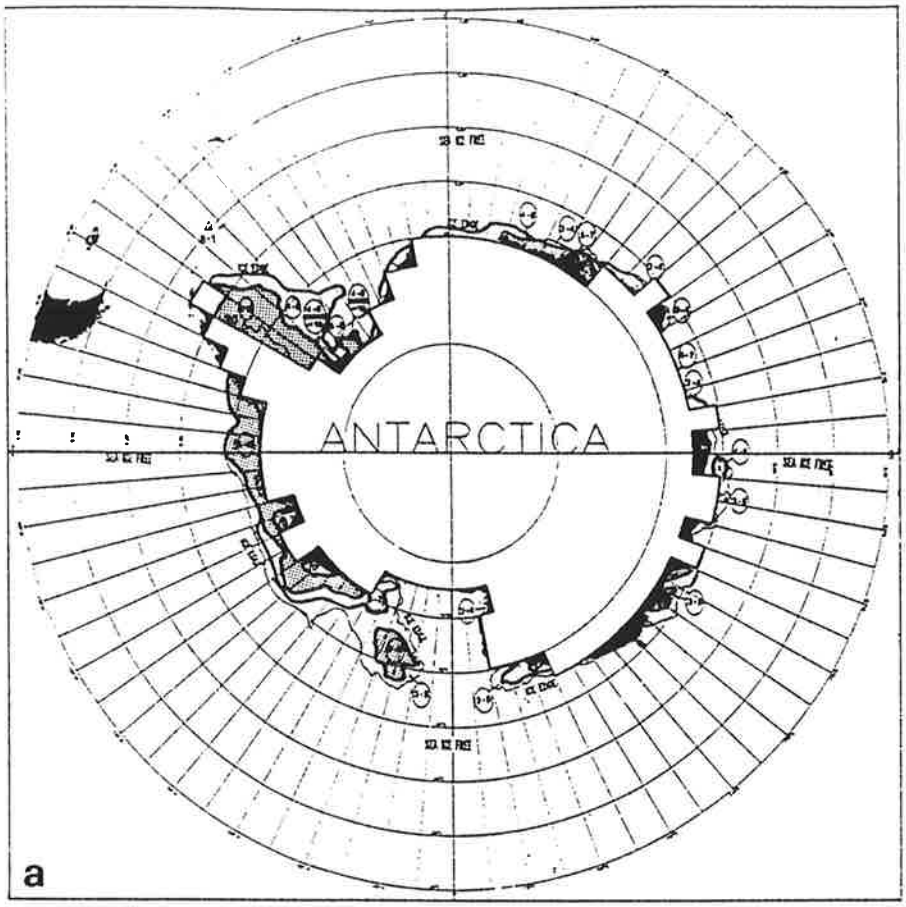

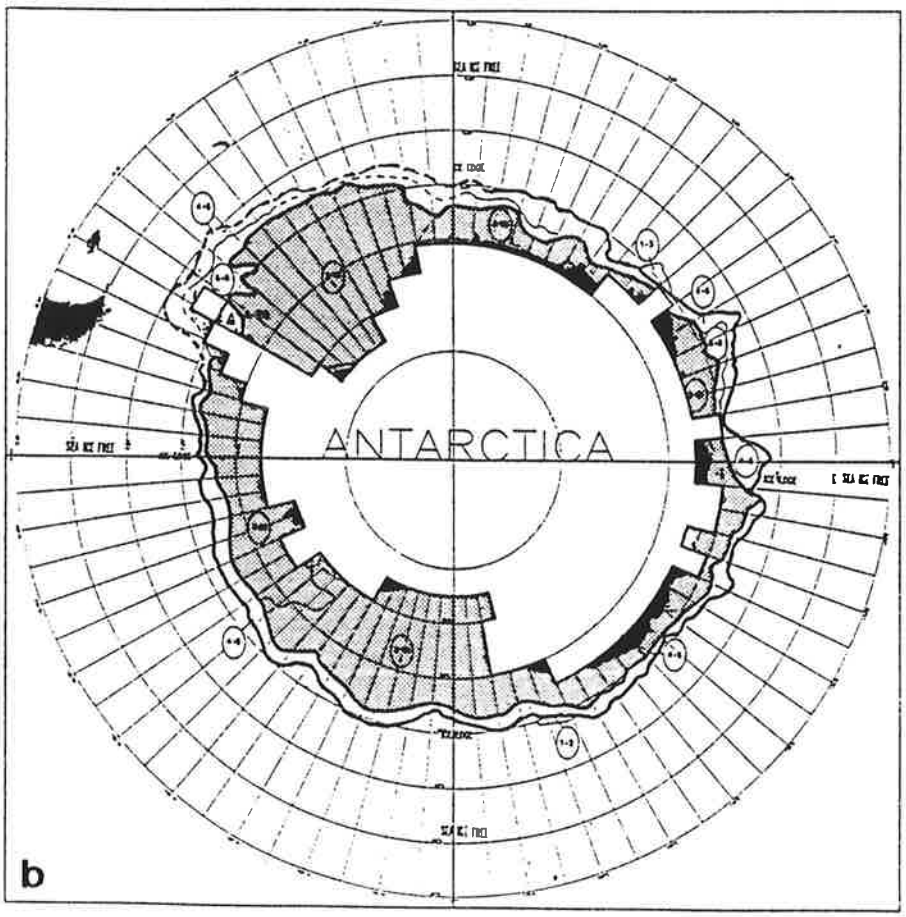

20 % ≤ N_i < 50 %

50 % ≤ N_i < 80 %

80 % ≤ N_i

fast ice, shelf ice or shore

Fig. 10

(Text see page 53)

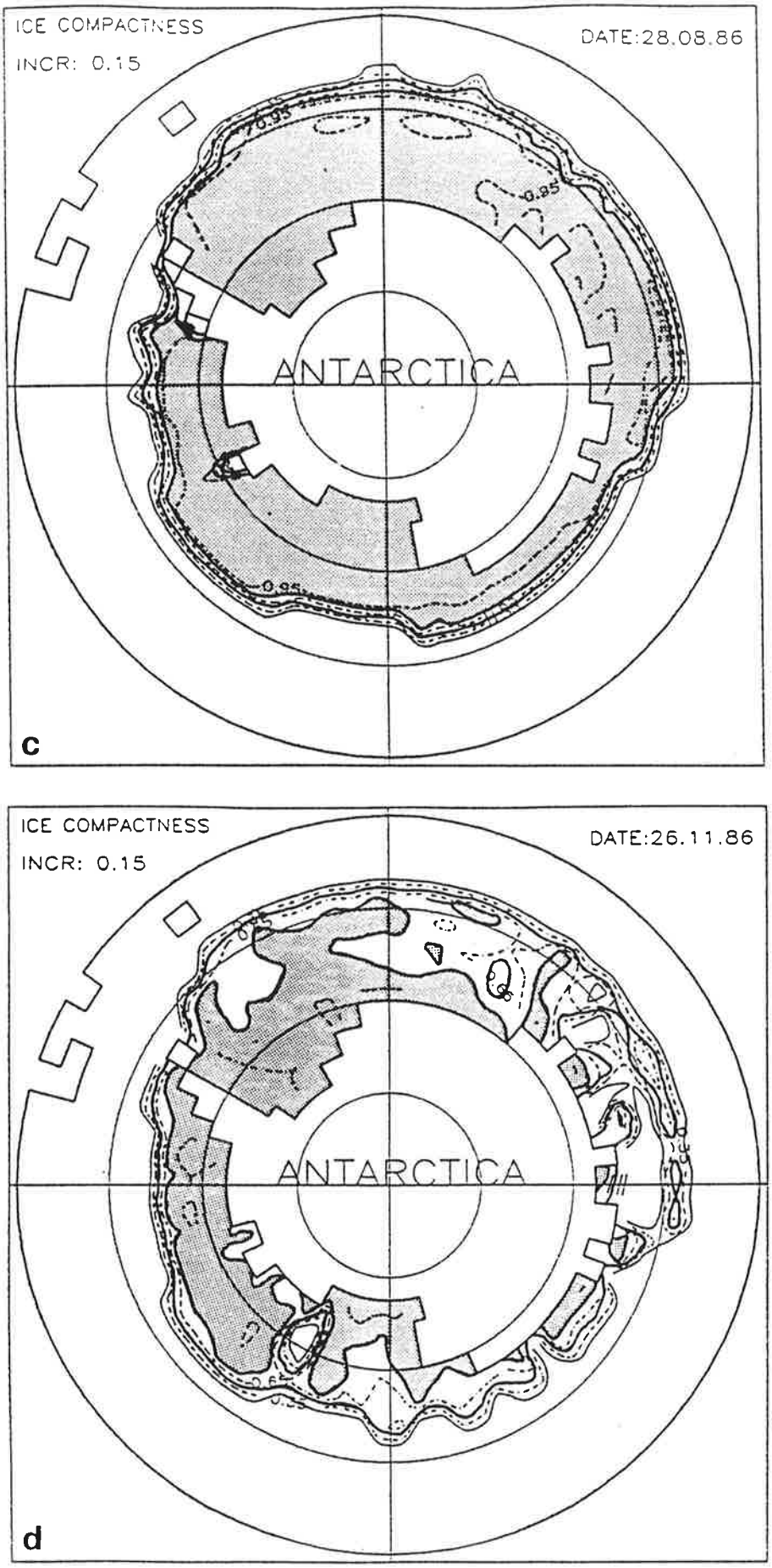

Fig.9: Contours of the real-time ice concentration from the same model version as in Fig.8, representing the specifically indicated dates.

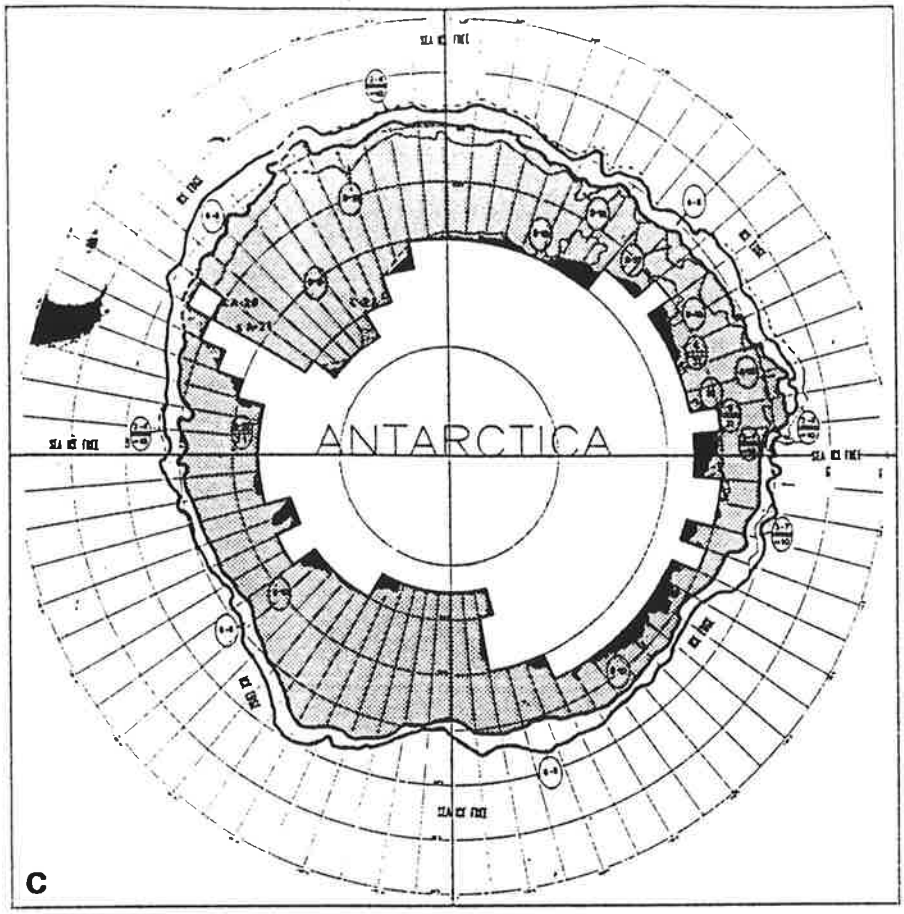

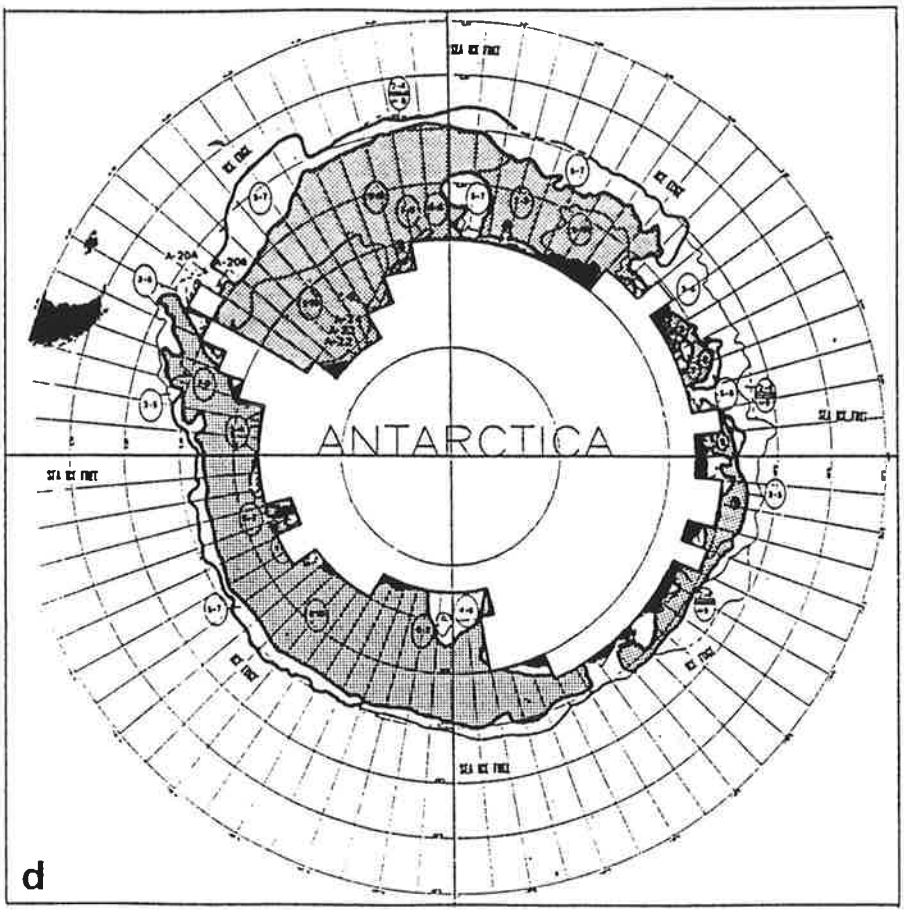

Fig.10: Contours of the real-time ice concentrations according to the Navy/NOAA Joint Ice Center based on observations and satellite data, representing the same dates as in Fig.9.

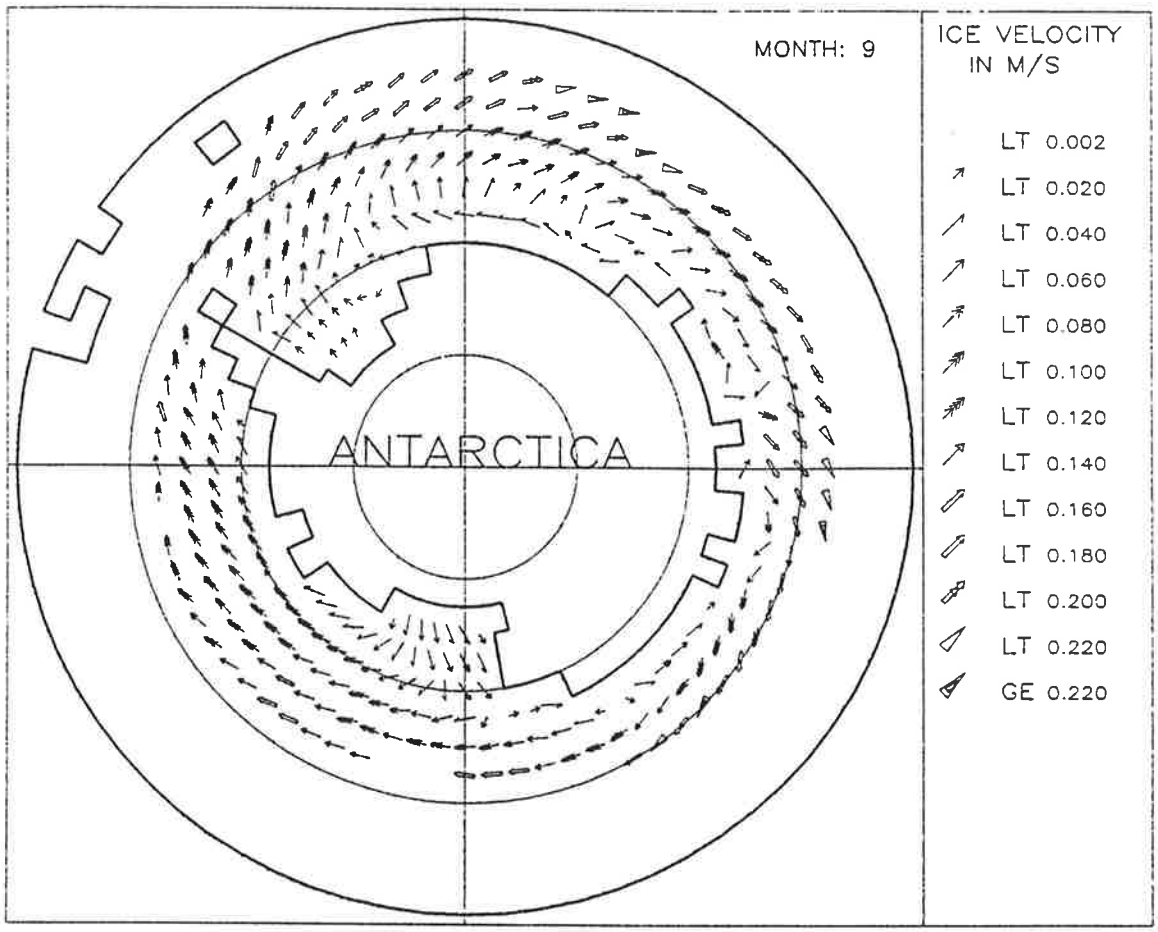

Fig.11: Monthly mean ice velocities from the same model version as in Fig.8, representing the same month as in Fig.3.b.

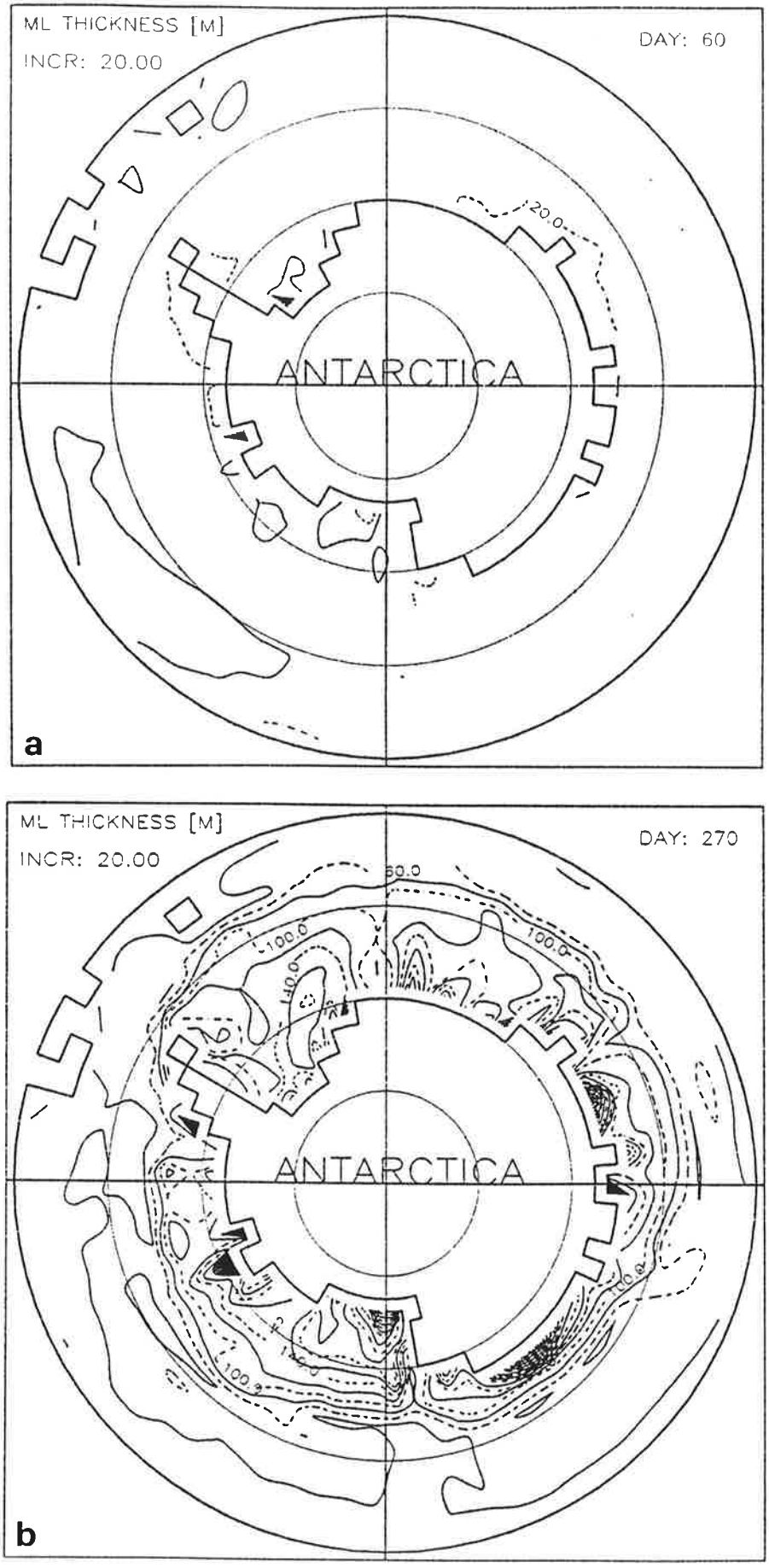

Fig.12: Contours of oceanic mixed-layer depth from the same model version and for the same dates as in Fig.8.

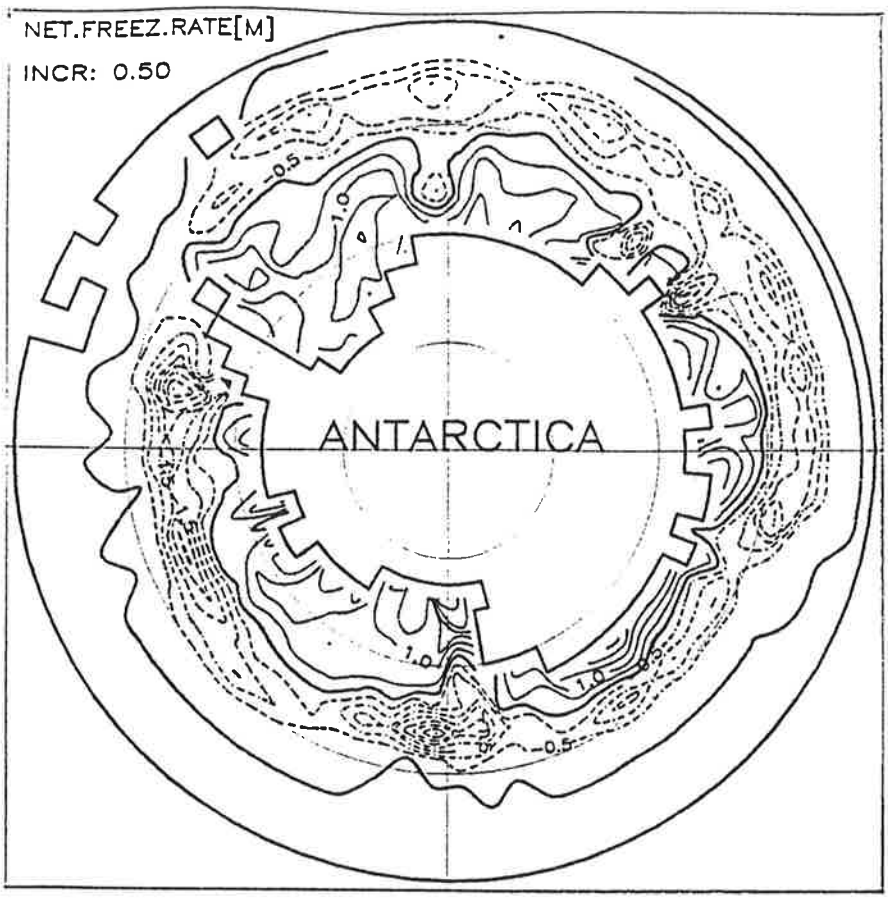

Fig.13: Net freezing rates from the same model version as in Fig.8; otherwise as Fig.7.

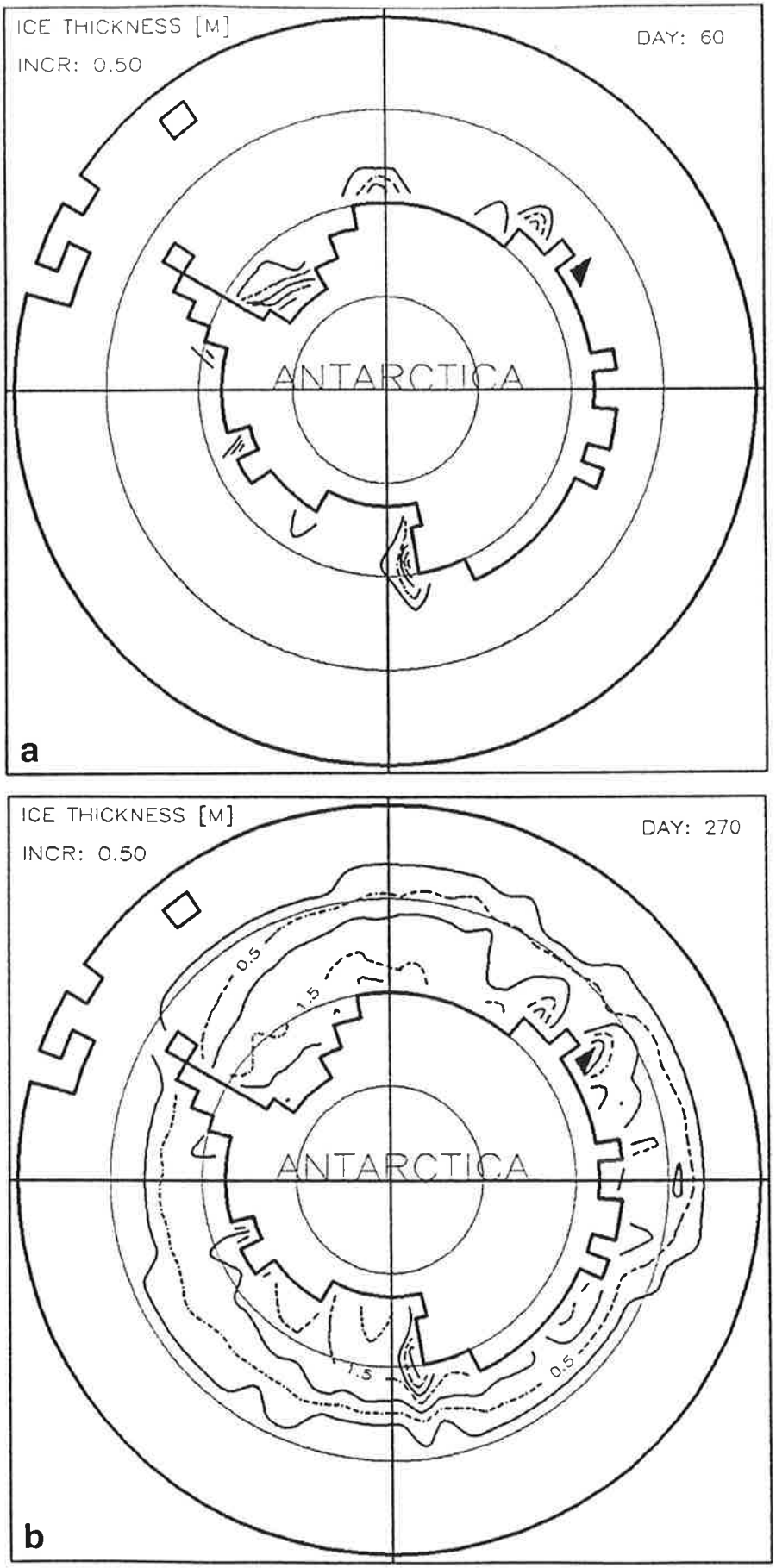

Fig. 14: Ice-thickness contours as simulated with the ABL – SI – OML model employing the 1000 hPa winds and a higher surface roughness, representing the same dates as in Fig. 2.

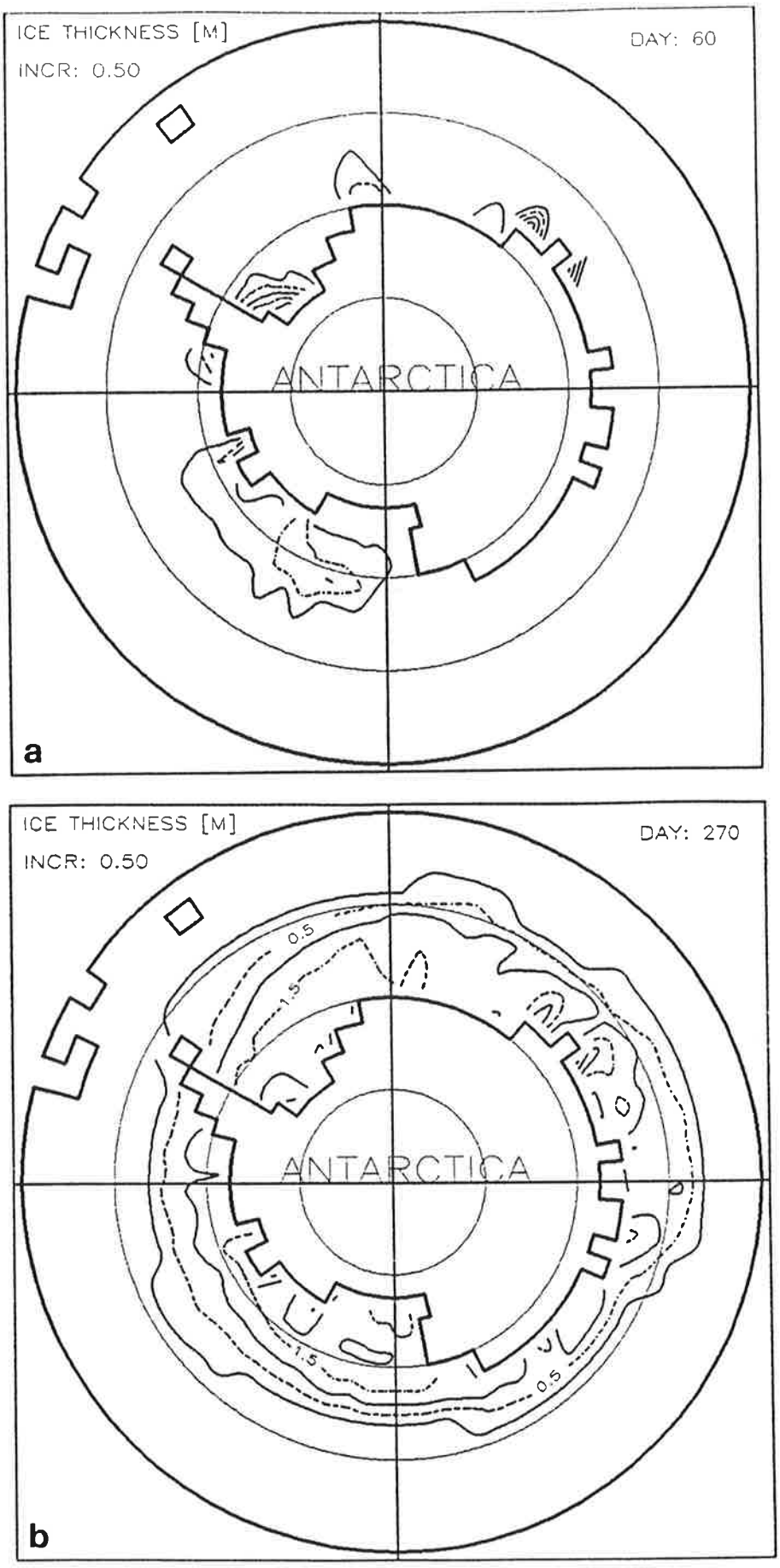

Fig. 15: Ice-thickness contours from the same model version and for the same dates as in Fig. 14, and with employment of additional wind turning.

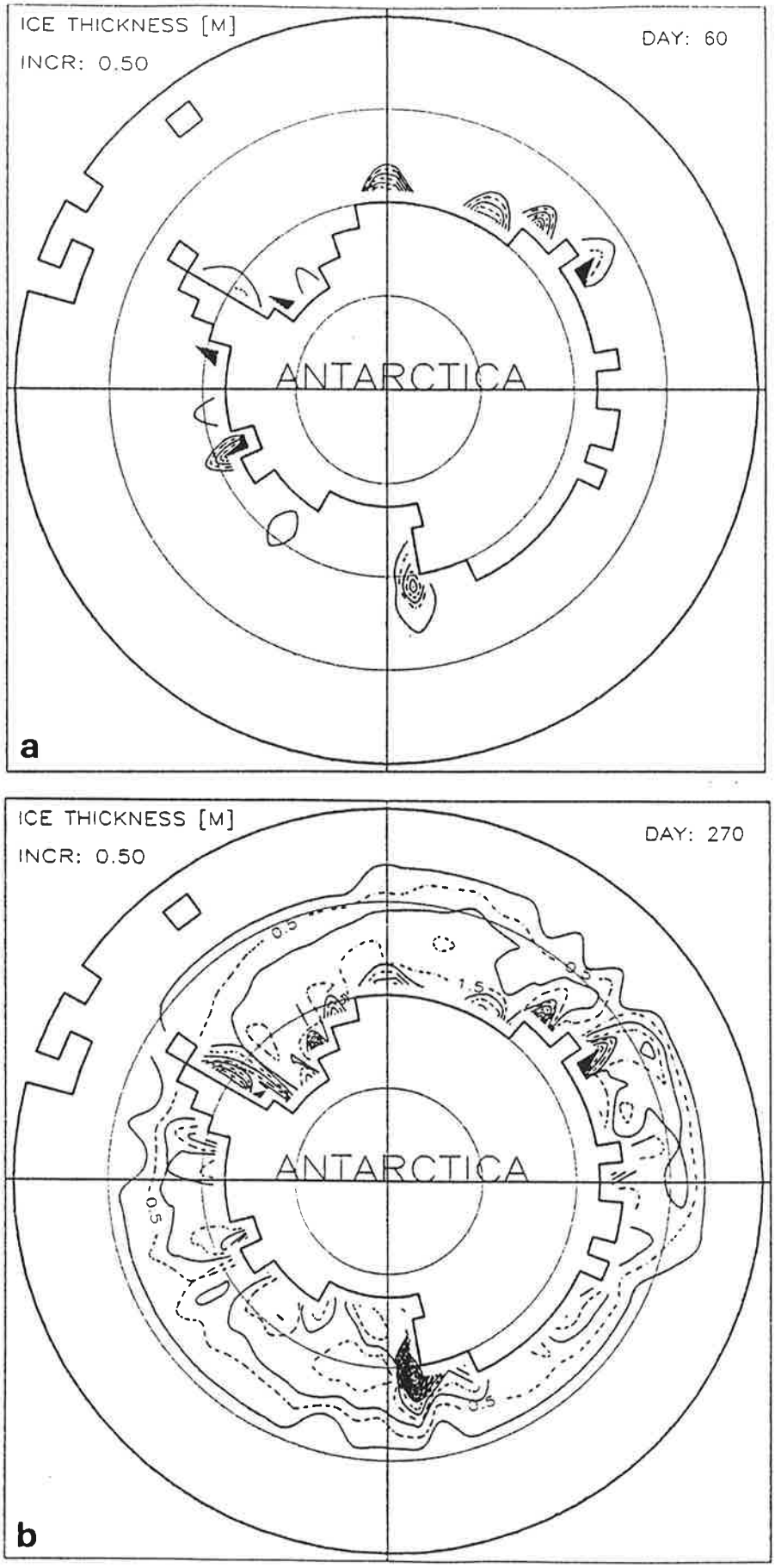

Fig.16: Ice-thickness contours from the same model version and for the same dates as in Fig.14, and with employment of higher buoyancy fluxes.

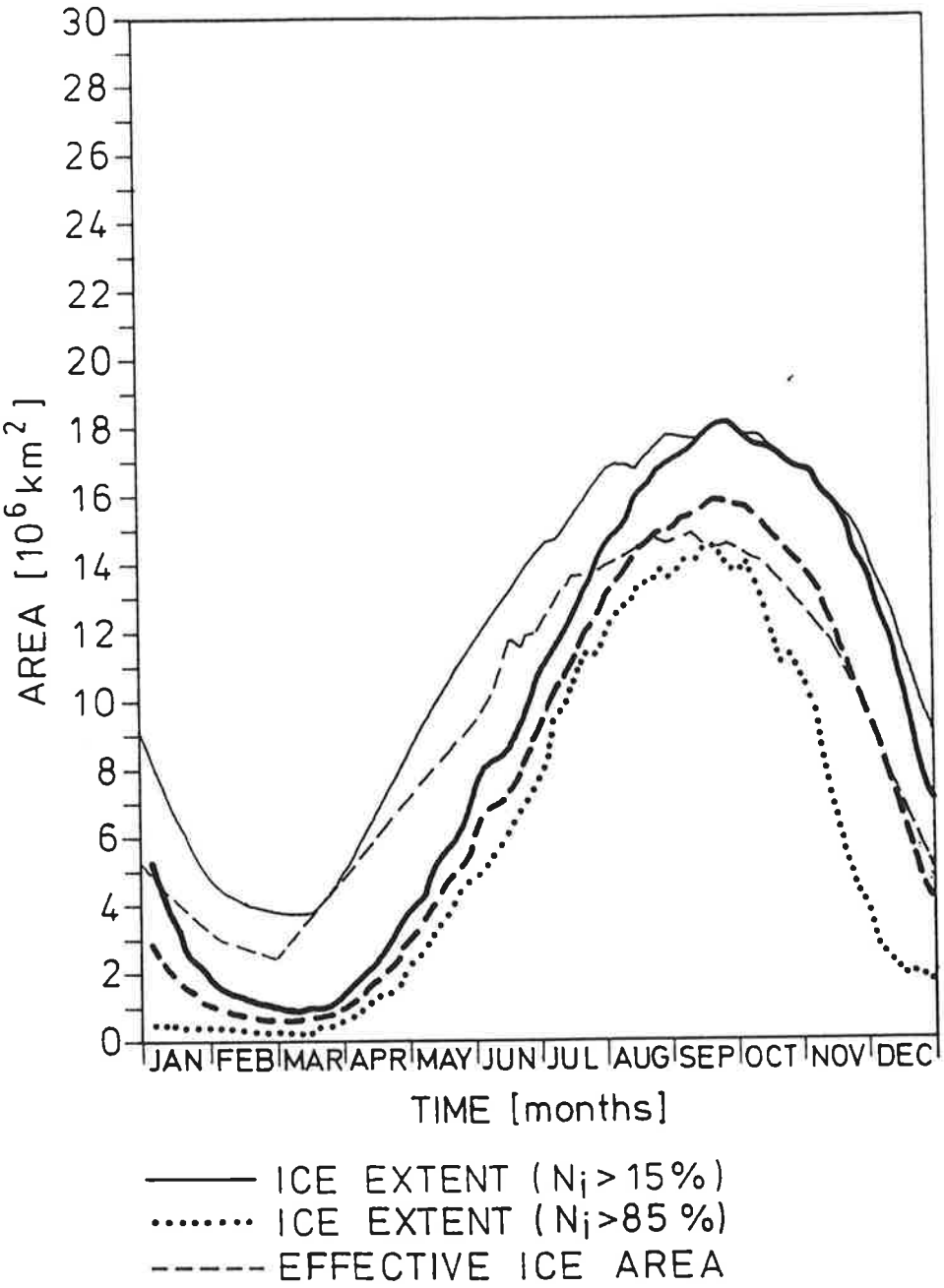

Fig. 17: Seasonal cycles of ice extent and effective ice area simulated with the same model version as in Fig. 16 (thick curves), and derived from SMMR data according to Gloersen and Campbell (1988) (thin curves), respectively representing the year 1986.

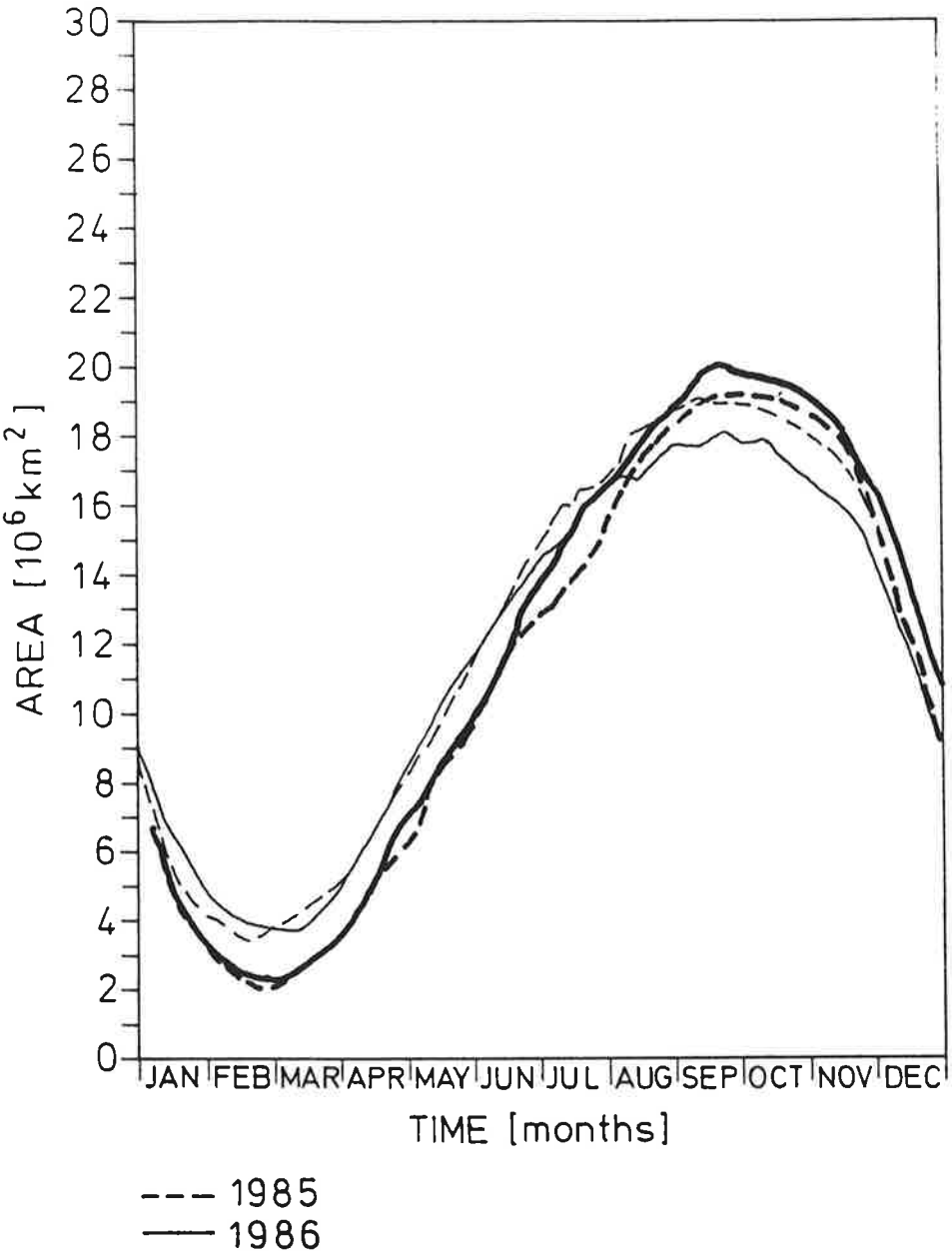

Fig. 18: Seasonal cycles of ice extent simulated with the ASL – SI – OML model (thick curves), and derived from SMMR data according to Gloersen and Campbell (1988) (thin curves), for 1985 (dashed curves) and 1986 (full curves), respectively.

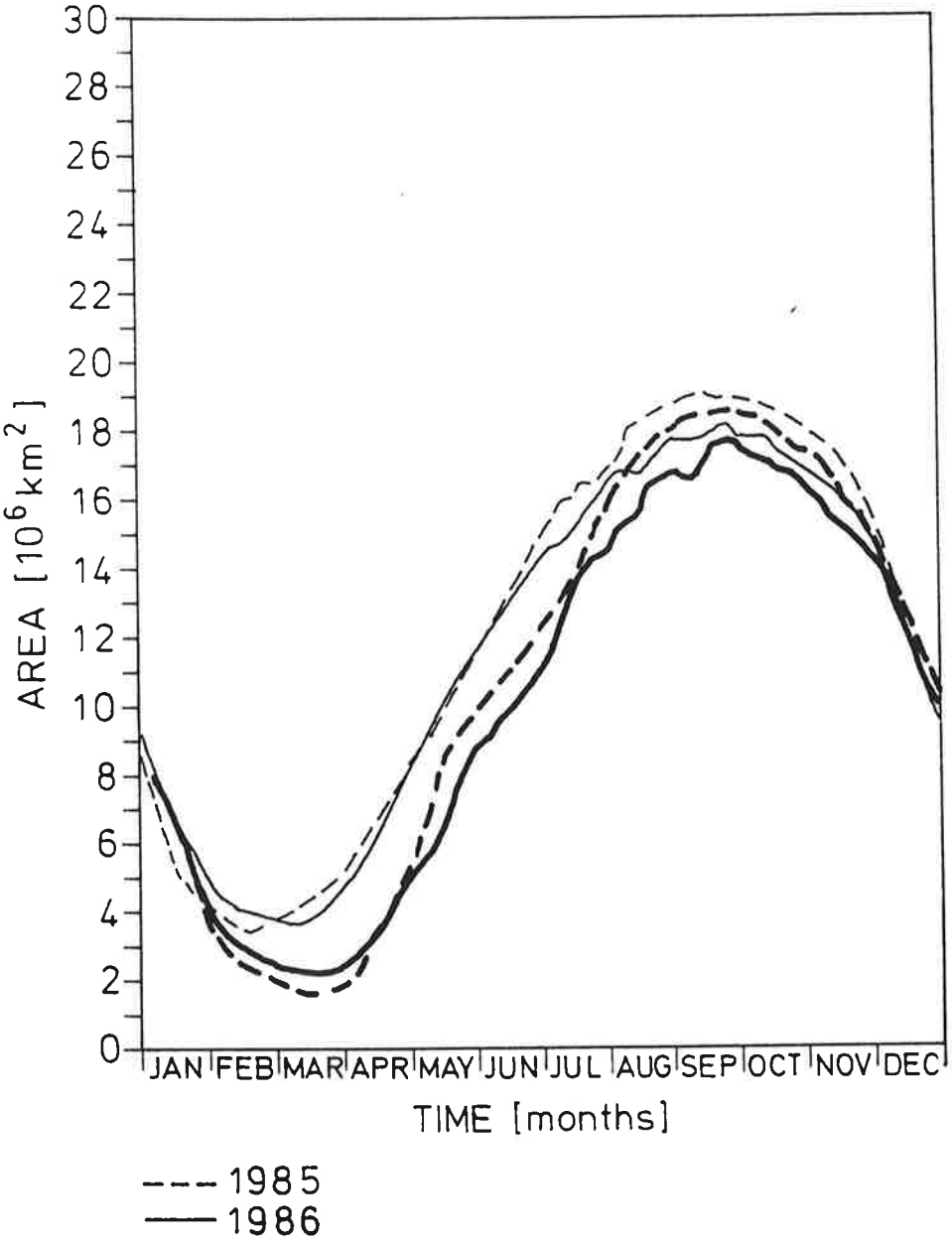

Fig.19: Seasonal cycles of ice extent from the same model version as in Fig.16, and with employment of additional wind turning (thick curves), otherwise as Fig.18.

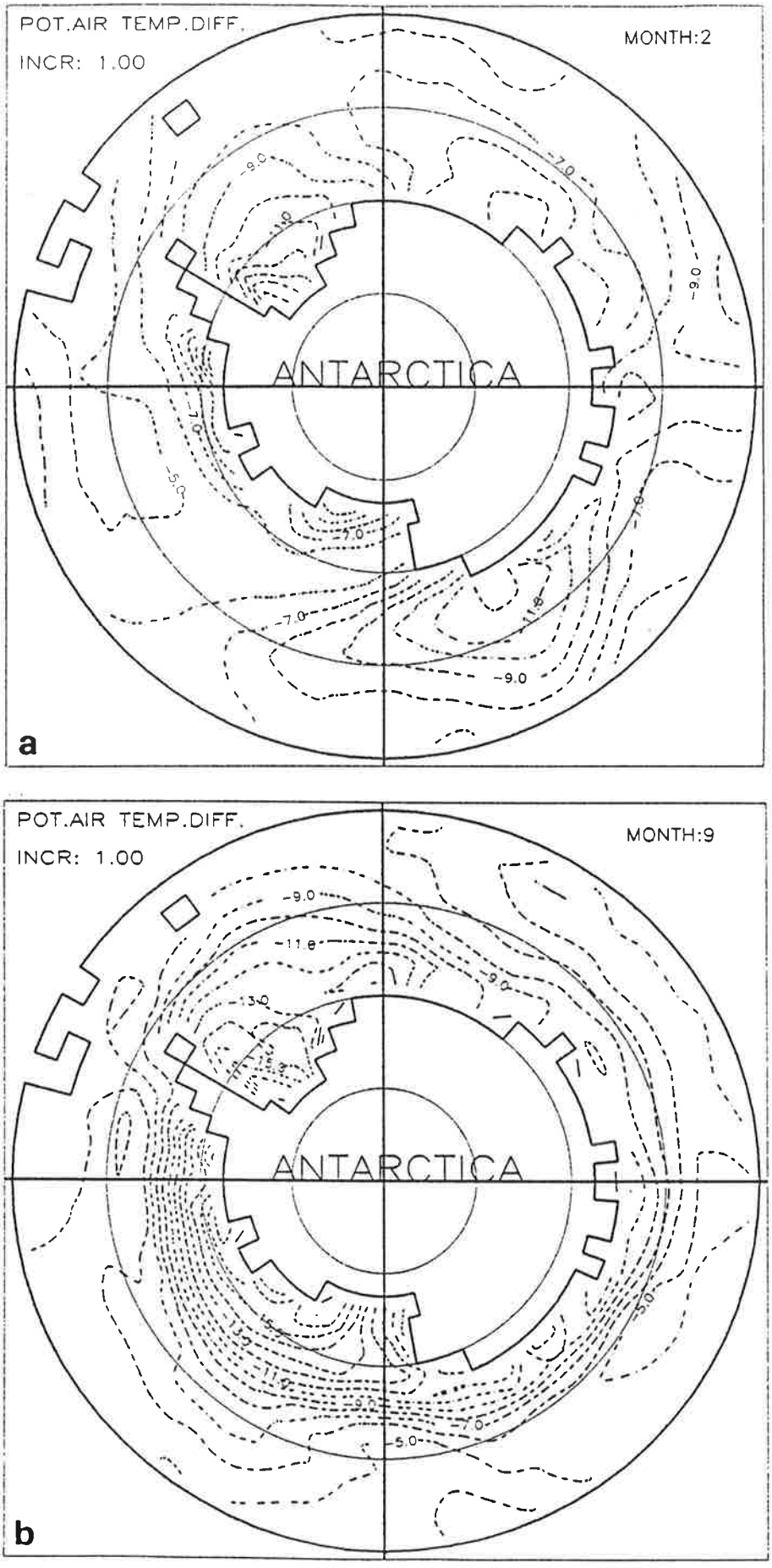

Fig.20: Differences of potential temperature between 1000 hPa and 850 hPa of the global analyses of the ECMWF, representing monthly means of February (a) and September (b) 1986.